UNIVERSIDADE DA BEIRA INTERIOR
Engenharia

Stress-Strain Relationship Characterization of Armoured Graded Aluminium and Steel Alloys Using a Digital Image Correlation Technique

(versão corrigida após defesa)

Hugo João Mendes Prata Graça

Dissertação para obtenção do Grau de Mestre em
Engenharia Aeronáutica
(ciclo de estudos integrado)

Orientador: Prof. Doutor Pedro Vieira Gamboa

Covilhã, Julho de 2018

Dedicatory

I dedicate this work to my family, in particular my parents, for given me uninterrupted support through everything and instilling in me the thirst for knowledge. I would also like to dedicate this work to my cousin Vasco, with whom I grew up with and for unfortunate circumstances is no longer with us.

Acknowledgement

For the development of this work several people, through greater or smaller degree of involvement, were important in enabling its completion and to whom I express my acknowledgments.

On a special recognition, I would like to denote and thank those of whom were crucial:

In first place to Professor Doutor Pedro Vieira Gamboa (UBI), scientific coordinator of this study, for his support and dedication, both with the experimental work and mentoring in the realization of this dissertation.

To Professor Doutor Paulo Reis (UBI), Professor Doutor Paulo Fael (UBI) and Professor Doutor Abílio Silva (UBI), for their help with the planning and experimental execution, as well as the important advice given.

To CEiiA (Centre of Engineering and Product Development) the head of the project and without it, this work would not have been possible and in particular, Doctor Pedro Talaia for his mentoring and guidance.

To every member of Departamento de Ciências Aeroespaciais, professores and employees, that made possible this achievement, as well as supporting the completion of this work.

To all my colleagues and friends for their help and support throughout this journey.

Finally, to my family for all their support and specially my parents whom were tireless throughout all my academic journey, and without whom nothing would have been possible.

Abstract

The need for better and lighter armoured concepts is ever increasing. Weather due to the challenges of the modern theatre of war, which require the vehicles to easily move in dense urban areas and in vast soft grounded deserts, or by the nature of the increasingly ingenious threats, traditional armour solutions fail to provide adequate protection.

The current work is part of a project intended to develop an armour solution that incorporates cork in its composition. This work focuses on the study of metal alloys and their mechanical characterization at low strain rates. For this purpose, a look is taken into the history and evolution of armoured vehicles and the characteristics of the different materials adopted in the course of armour development. The basic concepts associated with metal alloys loading and deformation behaviour are described as well as the methodology usually employed when preforming mechanical characterization of metals.

In order to determine the material constants required to create the strain hardening parameter of the Johnson-Cook constitutive material model, quasi-static tests are conducted in 45 specimens composed of three rolling directions (0º, 45º and 90º) of 5 mm and 10 mm thick AW-5083-H111 aluminium alloy and 2.2 mm thick Ramor 500 steel alloy. The strain data is processed through strain gauges applied in the specimens' surface and an in-house integrated digital image correlation technique.

The experimental results show that the digital image correlation technique employed in this study offers good results compared to both the strain gauge data and the similar examples from the literature. It is also possible to note the difference in behaviour in the three cutting directions in both alloys. Dynamic strain aging and instabilities of high frequency oscillation phenomena are recorded on the aluminium alloy, just as expected from high magnesium content alloys. The strain hardening constants and the Cockcroft-Latham failure criterion are successfully extrapolated and compared to similar materials. As a general conclusion, this work creates a good foundation for the full material characterisation on the larger spectrum of strain rates and will allow for the future research necessary for the main project.

Keywords

Armour, Ballistic Impact, Tensile tests, Digital Image Correlation, Constitutive Models.

Resumo Alargado

A necessidade para melhores e mais leves conceitos de blindagens é sempre crescente. Quer devido às dificuldades do campo de batalha moderno, que requerem que os veículos se movam facilmente nas densas áreas urbanas e em vastos desertos de terreno macio, quer pela natureza crescentemente engenhosa das ameaças, as blindagens tradicionais falham em fornecer proteção adequada.

O presente trabalho, faz parte de um projeto com o propósito de desenvolver uma solução de blindagem que incorpore cortiça na sua composição. Este estudo irá focar-se em ligas metálicas e a sua caracterização mecânica a baixas taxas de deformação. Para este fim, é feita uma breve revisão da história e evolução de veículos blindados e as características dos diferentes materiais empregados no desenvolvimento de blindagens. Os conceitos básicos associados com o comportamento de carregamento e deformação de ligas metálicas são descritos assim como a metodologia normalmente utilizada aquando da execução da caracterização mecânica de metais.

A fim de determinar as constantes do material necessárias para a criação do parâmetro de endurecimento de deformação do modelo constitutivo de material de Johnson-Cook, são realizados testes quase estáticos em 45 provetes compostos pelas três direções de rolamento (0º,45º e 90º) de alumínio AW-5083-H111 de 5 mm e 10 mm de espessura e aço Ramor 500 de 2,2 mm de espessura. Os dados da deformação são processados a partir de extensómetros aplicados na superfície dos provetes e por uma técnica de correlação digital de imagem caseira.

Os resultados experimentais mostram que a técnica de correlação digital de imagem empregada neste estudo oferece bons resultados quando comparado com os dados dos extensómetros e com exemplos de materiais semelhantes da literatura. Também é possível denotar o comportamento diferenciado nas três direções de corte em ambas as ligas. Os fenómenos de envelhecimento dinâmico da deformação e instabilidades de oscilação de elevada frequência são registados na liga de alumínio, tal como esperado de ligas de elevado teor de magnésio. As constantes do endurecimento da deformação e do critério de falha de Cockcroft-Latham são extrapoladas com sucesso e comparadas com materiais semelhantes. Como conclusão geral, este trabalho cria uma boa fundação para a completa caracterização dos materiais num maior espetro de velocidades de deformação e vai permitir realizar a investigação necessária para o projeto principal.

Palavras Chave

Blindagem, Impacto balístico, Testes de tração, Correlação Digital de Imagem, Modelos Constitutivos.

Table of Contents

List of Figures

List of Tables

List of Acronyms

AP	Armour Piercing
ASTM	American Society for Testing and Materials
CEiiA	Centre of Engineering and Product Development
C-L	Cockcroft and Latham
DSA	Dynamic Strain Aging
DIC	Digital Image Correlation
J-C	Johnson and Cook
U.S.	United States of America
WWI	First World War
WWII	Second World War

List of Symbols

$\dot{\varepsilon}_0$	Quasi-static tensile test strain rate
$\bar{\varepsilon}_I$	Average axial strain
$\dot{\varepsilon}_p^*$	Dimensionless plastic strain rate for $\dot{\varepsilon}_0$
A_0	Specimen´s initial cross-sectional area
A_R	Specimen's cross-sectional area
C_B	Bridgman's analytical correction factor
C_O	Ostsemin's analytical correction factor
D_{1-5}	Johnson and Cook cumulative damage model constants
F_s	Force parallel to the surface
T_H	Homologous Temperature
T_m	Material's melting temperature
T_r	Room temperature
W_{cr}	Critical value of W
a_0	Specimen's initial half-thickness
x_0	Initial length
$\bar{\varepsilon}$	Effective strain
$\dot{\varepsilon}$	Strain rate
ε^f	Strain to fracture
ε_n	Engineering strain
ε_t	Transverse strain
ε_x	Strain in the specimen's length
ε_y	Strain in the specimen´s width
ε_z	Strain in the specimen´s thickness
ε_ρ	Amount of plastic strain
σ^*	Dimensionless pressure/stress ratio
σ_1	major principal stress
σ_H	Hydrostatic stress
σ_T	Average true stress
σ_Y	Johnson and Cook stress flow equation
σ_{eff}	Effective stress
σ_n	Engineering stress
σ_x	Stress in the specimen's length
σ_y	Stress in the specimen's with
σ_z	Stress in the specimen's thickness
τ_{xy}	Shear stress between length and width
τ_{yz}	Shear stress between width and thickness
τ_{zx}	Shear stress between thickness and length
$\Delta\varepsilon$	Plastic straining
A	Material yield strength
B	Strain hardening constant
C	Strain-rate constant
D	Johnson and Cook cumulative damage model
E	Young's modulus
F	Force
L	Specimen's original length
R	Radius of curvature of the surface of the neck
T	Absolute temperature

U	Strain Energy
W	Strain energy per volume unit
a	Half-thickness of the neck
a'	Half-thickness at location b
dx	Increment in deformation
$d\varepsilon$	Increment of true strain
m	Thermal softening exponent
n	Strain hardening exponent
x	Current length
ε	True strain
σ	True stress
τ	Shear stress
υ	Poisson's Ratio

1 Introduction

1.1 Motivation

The need for lighter armoured vehicles on the modern battlefield is demanding a constant search for new and more effective light weight armour solutions. This work is part of the Light Armoured Multi-Purpose Vehicle (L-AMPV) project lead by the Centre of Engineering and Product Development (CEiiA) in conjunction with the Portuguese Defence Ministry, Universidade de Aveiro and Universidade da Beira Interior, for which the goal is to develop an armour solution incorporating cork.

The significance of this project lies with the necessity of reducing the weight of current armour solutions while increasing their effectiveness and maintaining the production costs low. Cork is a low density, natural, renewable and ecological material with great abundance in Portugal. Previous studies indicate that this material exhibits interesting damage absorption properties, in both low and high impact speeds when applied in sandwich structures [1, 2, 3, 4]. In addition to the damage resistance, cork also offers good thermic and acoustic insolation, vibration absorption and suppression and fire resistance characteristics, indicating exceptional properties for armour application. Due to the diversity of the present-day threats, several layers of materials are usually incorporated in effective armour solutions, each with a specific function to defeat ballistic and blast wave impacts. Therefore, the suitable selection and study of current available armour solutions is fundamental to achieve the best combination of materials that will enhance the strong suits of each layer while minimizing their weaknesses without creating a prohibitively expensive solution.

The correct material characterization is a fundamental step for the ability to appropriately execute numerical simulations capable of providing acceptable data and inexpensively test material combinations and armour solutions. This is dependent on good experimental data that is often expensive and time consuming, especially when several materials are the subject of study. In order to turn the task into more manageable portions, each partner is responsible for the study of smaller combination of materials suited to their available resources.

1.2 Objectives

The current work will focus on the mechanical characterization of the armour graded aluminium and steel, available for the project, at low deformation rates.

For this purpose, a literature review, including the historical evolution of several armour solutions used through time, is necessary to comprehend the available alloys but also for the materials available for the project in order to understand the important characteristics and behaviours thought out when designing armour solutions.

It will also be sought to understand the methodology involved in the execution of tensile testing and the characterization of metals, including the best techniques to analyse the material behaviour up to rupture.

Test and compare the results of the two armoured graded alloys, AW-5083-H111 aluminium and Ramor 500 steel, in three different directions of rolling, and the effect of thickness in the materials behaviour to quasi-static tensile tests, with the goal of the subsequent creation of constitutive mechanical models of the materials.

These tests will form the basis for all the future characterization of the materials which will allow the execution of numerical simulations intended to find the best armour solution.

1.3 Structure of the Work

This work is constituted by five main chapters, beginning with the current introduction, followed by the literature review, where the evolution and current armour solutions are compiled. An introduction of the necessary concepts required to successfully understand and conduct the quasi-static material testing as well as the data required for the correct development of the tested materials constitutive models will also be described in this chapter.

The third chapter will be an overview of the conducted experimental studies, namely the manufacturing process and specimen preparation, the used equipment and a detailed description of the experimental procedure. In the next chapter, the experimental results are compiled and analysed for the different materials and thicknesses. A final interpretation and comparison of the results with similar materials on the literature is also conducted.

The culmination of the investigation is found on the fifth chapter, with the conclusions made from all the realised experimental work and the proposed procedure for the full material characterisation including the higher deformation speeds.

2 Literature Review

2.1 Armoured Fighting Vehicles

The objective of this section is to expand the knowledge of the history and development of Light armoured vehicles, as well as the different designs used to defeat the different threats faced.

The origin of the first armour is very hard to trace, for as long as there was war, there was the need for defence. When it comes to fighting vehicles, their use can be traced to war chariots used as far back as in 1700BC in the Middle East, first as battle taxis, and later as mobile weapons platforms.

During the Middle Ages wheeled siege towers were used to offer protection to the crews and soldiers while moving toward the enemy fortifications. However, Leonardo Da Vinci's 1487 sketch of a mobile, protection gun platform is frequently cited as the prototype of modern tank, Fig 1, [5].

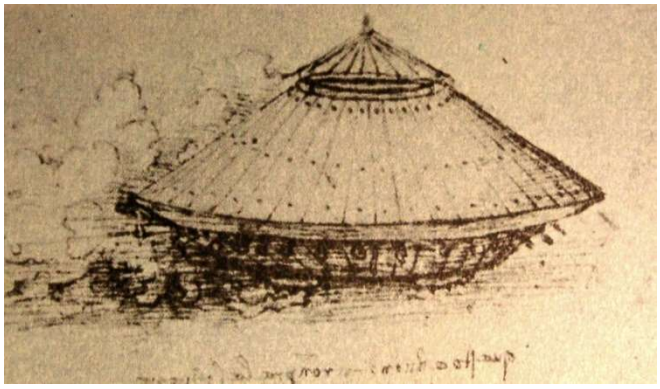

Figure 1: Pen Drawing of Armoured Car by Leonardo Da Vinci 1487, [5].

But it was only with the invention of the traction engine and the motor car in the beginning of the 20th century that allowed the idea of the armoured vehicles, as it is recognised today, to take shape.

The first armed vehicle was a De Dion-Bouton quadricycle on which F. R. Simms mounted a Maxim machine gun in 1899 [6], whereas the first armoured vehicle was a road locomotive designed by F. R. Simms and built by Vickers, Sons and Maxim, Limited, in 1902, for the defence of the British Coast [7].In 1903 a French artillery officer, captain Levavasseur, put forward a scheme for a self-propelled 75mm gun on an armoured tracked chassis. The scheme was considered by the French Artillery Technical Committee, but the latter came to the conclusion that animal traction was preferable for guns and finally rejected the scheme in 1908. Similar concepts are recorded in several countries during the same period, however, all had similar fates [8].

During the First World War (WWI), all of that changed, and the necessity for a vehicle that could traverse a mud and shell cratered battlefield, break through the wire fortifications and overcome trenches in order to engage the enemy, lead to the creation of the Lincoln Machine, also known as, Little Willie, in 1915. This was the first tracked vehicle, that, contrary to the wheeled counterparts, could cross the battlefield without getting stuck, [9].

2.1.1 Steel

The advent of the tank, as known today, only truly came to fruition during WWI with the British Mark I, the first fighting tank [10]. This tank set out the basic blue print from where the future fighting vehicles would build upon. The first tanks were armoured purely with steel, which for some time was the material of choice, when it came to the design of armours, due to the availability of a large technological database, relative cheap costs of production and wide range of mechanical properties [11].

When it comes to ballistic impacts the most critical property affecting steel's performance is its hardness [12]. With increasing steel hardness, there is a significant decrease of the penetration and propagation of the projectile [11]. With low hardness levels steel, the projectile core passes intact through the armour forming a ductile hole but with very high hardness levels fracturing of the steel target upon impact may occur making it shatter [11, 12].

When a projectile hits' the target material, compressive stress waves occur firstly. After that, these compressive waves reflect back from the rear side of the material as tensile waves and finally the interaction of these waves cause crack initiation, crack propagation and failure. In order to handle these waves, strength and toughness of the target material should be high [13, 14].

Another important aspect of steel armours is the fact that, in many cases, it is very hard to produce a monolithic plate with the desired thickness, which results in the use of multi-layered plates. There is extensive literature regarding the effects of double layered target plates, with and without spacing, but with many contradicting results. For instance, Gupta and Madhu [15] performed an experiment on ballistic performances of single and multi-layered plates of mild steel, rolled homogeneous armour and aluminium against 6.2mm projectiles having a velocity range of 800-880 m/s. They found that although two layered thick plates had similar ballistic performance with the single plates of equal thickness, further increasing the number of layers decreased their ballistic resistance. A similar conclusion was reached in numerical models by Flores-Johnson and Edwards [16]. They found better ballistic performance in monolithic plates, though the effect diminished with increased impact velocity. On the other hand, S. Dey et al. [17] tested the ballistic resistance of double layered steel plates and found an overall increase in the ballistic limit velocity in the double layered targets.

However, the main drawback of steel armours is its density. With the ability to incorporate larger weapons and engines in tanks, and with development of better tank counter measures,

a constant increase in weight and reduction of mobility was unavoidable, culminating in the Second Wold War's (WWII) Maus (mouse) tank. This super heavy tank design would have weighed 188 tonnes and with an armour up to 2400 mm thick, it would not have been able to even cross bridges, and no engine available could give it a reasonable speed [18].

2.1.2 Aluminium

One lighter alternative to steel is aluminium, and in the 1950's the American M113 APC was the first armoured vehicle fabricated from AA-5083 aluminium and it was the most widely used United States of America (U.S.) Army armoured vehicle in the Vietnam War. The application of the aluminium armour made the vehicle lighter than its predecessors, moderately amphibious, air transportable and air droppable, but was strong enough to protect its crew against small arms fire. Aluminium was chosen because, for protection against 7.62 mm AP (armour piercing) and 14.5 mm AP, the areal density required of some aluminium alloys is lower than their steel counterparts [18].

When it comes to damage mechanisms and energy absorption, aluminium follows a very similar pattern to steel, so that many of the experiments mentioned above where preformed both in steel and in aluminium. It was found that, like steel, the higher its level of hardness the better at resisting impacts it becomes [14]. In [15, 16] it's found that more layers decrease ballistic performance, though, if paired as a front face with steel backing, this hybrid solution was the best double layer ballistic performer [16]. Because, the level of hardness of aluminium cannot compete with steel, it becomes necessary, to face modern threats, to combine it with other materials. This lead to the development of composite armours.

2.1.3 Composites

In an attempt to face new anti-tank threats, such as shaped charges and high-explosive (HEP) rounds, in 1952, the development of a siliceous cored armour was initiated. It consisted of fused silica glass sandwiched between rolled steel plates, and it proved to be significantly more effective than plain steel armours [19]. Though it was never used, because the vehicle in which it was meant to be applied never went into production, it served as concept for future armour developments.

Nowadays, composite armours have become much more sophisticated and complex, with several different layers, each with a specific function in defeating a projectile. Many mechanisms are used in composites to stop a projectile. These usually include [20]:

1. Projectile deformation and fragmentation,
2. Projectile deceleration and controlled moment transfer to the target,
3. Projectile and armour spall shield.

Different materials are used to exploit each mechanism:

1. A high hardness (and ideally tough) material such as alumina, silicon carbide and boron carbide ceramics.

2. High strength, but fracture resistant for projectile deceleration through plastic energy dissipation, such as steel, aluminium and titanium.

3. High strength fibres in textile or composite form, such as Kevlar®, glass fibre reinforced polymers and ultra-high molecular weight polyethylene (UHMWPE),

There is a myriad of materials that can fulfil these requirements, but for the sake of simplicity only the materials available for this project (steel, aluminium, alumina, glass fibre/phenolic resign reinforced polymers) are addressed.

2.1.4 Ceramic

The first battle use of ceramic armour technology was in U.S. helicopters during the Vietnam conflict where low-level sorties made the helicopter and crew vulnerable to small-arm fire. It was the most weight-efficient means of providing protection and was applied in air crews' vests and around the seats [18]. However, the first patents for a ceramic-based armour were filed by the Goodyear Aerospace Company in 1963 and granted in 1970 [21].

In the 1980s, the majority of the ceramic-based armour systems that were deployed in the battlefield applications used alumina. Alumina (Al_2O_3) is relatively inexpensive to manufacture, and even quite thin sections can stop high-velocity small-arms bullets [18].

The main anti-ballistic mechanisms observed in ceramics involve an initial stage where the projectile gets its tip blunted. At the same time a crack is initiated in the rear surface of the ceramic as the back-plate yields in their interface. This crack is usually conical in shape with its base with a diameter twice as large as the ceramic thickness, which helps spread the area of impact in the back plate. In the second stage, the ceramic turns to rubble as the projectile is eroded. Approximately 40% of the projectile mass and initial energy are carried off by eroded projectile material. In the last stage, the erosion of the projectile ceases and the remaining energy and spall are absorbed by the back plate [18, 22, 23, 24, 25, 26].

Though ceramics present several advantages against ballistic impacts, there are several drawbacks. They have very poor multi-hit impact response and are sensitive to transit and use due to their brittleness, they can be more difficult to manufacture than armour-graded metals and cannot be used for load-bearing structures.

2.1.5 Fibre Glass

The field of high-performance fibres is only about 60 years old. Nylon and silk fibres had been used to make armour vests for soldiers, but with very limited success. In the 1960s, DuPont developed polyparaphenylene terephthalamide, also known as Kevlar®, and it was able to

successfully stop a bullet [27]. Since then, Kevlar® has been used extensively in the design of body armour, and even as spall liner for some light armoured vehicles [18].

However, Kevlar® is very expensive to fully integrate in a vehicle armour while glass fibre reinforced polymers, either from E-glass or S2-glass, present a more cost effective alternative, having already been used in mine countermeasure vessels [28], and armoured fighting vehicles [29]. Though they cannot provide adequate protection on their own, combined with ceramics or high-hardness steels they can offer significant weight reductions. The role where these materials excel at are as spall liners and hard facing plates baking acting as a safety net to catch the debris from the initial impact while, in some configurations, also providing structural support [18].

2.1.6 Blast wave

Landmines have always been one of the most dangerous weapons. Since WWII more vehicles have been lost to landmines than any other threat [30], and with the recent conflicts in Iraq and Afghanistan the threat of landmines has been superseded by improvised explosive devices (IEDs) [31, 32]. The role of a well-designed armour is then to ensure that the magnitude of the pressure wave and its impulse, the length of the interaction time between the pressure wave and the structure, are controlled to keep any resultant stresses acting on the target below a critical threshold [33], as well as offer adequate protection against debris, shrapnel and fire [32].

In order to mitigate the effect of a blast, the general strategies that can be used in armour design are summarized next [33]. Impedance mismatch can control the transmitted pressure, by mitigating the peak pressure transmitted through the armour. Energy dissipation mechanisms can mitigate the transmitted impulse. Dispersion (and impedance mismatch) can increase the interaction time between the supported structure and the threat, so as to change the damage regime from one controlled by impulse to one controlled by pressure.

Typically, the energy of the stress waves induced by blast or impact is broadly distributed over multiple frequencies. Therefore, this energy must be tuned to a narrow spectrum before it can be optimally dissipated. This can be achieved by a multi-layer design in which the outer layers tune the stress waves to match the critical damping frequency of an inner viscoelastic layer. As a high-frequency stress wave travels through this viscoelastic layer, it undergoes multiple loading-unloading cycles which can result in significant energy dissipation over a short duration [33].

Some experiments have also indicated that a gradation (increase in density, from the impact face to the back face) of the material of higher acoustic impedance in the core of a sandwich structure helps reduce deflection and damage to the structure [34, 35].

2.1.7 Cork

When Cork, a natural material, is used as a core in sandwich structures, these sandwiches present high stiffness-to-weight ratio, high strength-to-weight ratio, excellent fatigue properties, thermal/acoustic insulation and corrosion and fire resistance [36]. With the need to produce lighter and more agile vehicles to face the modern battlefield demands, cork might present a good addition to current and future armour solutions.

Already some investigation has been done on the behaviour of core cork-based sandwich materials either for ballistic impacts [1] and blast waves [2, 3]. In the case of ballistic impacts, it was found that the presence of the cork core slightly increased the ballistic limit but strongly augmented the absorbed energy, while for blast waves, the sandwich thickness reduction indicated the possibility of energy dissipation by the cork, most probably due to the cork cellular structure crushing.

2.1.8 Composite Integral Armour (CIA)

One of the most advanced current armour solutions is the composite Integral Armour. This solution was designed to replace aluminium and optimize the weight and performance of an armoured vehicle for the U.S. Army.

This hybrid material consists of a ceramic strike face, a thin rubber layer and an S2 glass-based composite backing plate (Fig. 2). This solution has, so far, provided ballistic protection and structural integrity at the minimal areal-density [22]. The rubber layer between the ceramic tiles and the composite backing is used to increase the armour's multi-hit capability and structural damage tolerance by decreasing the stress wave transamination between the materials. [37, 38].

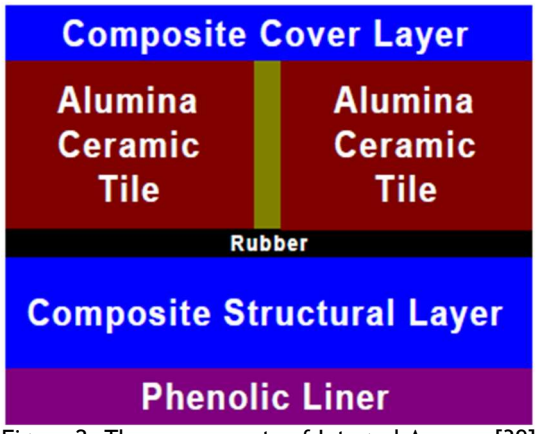

Figure 2: The components of Integral Armour [39]

As aforementioned, it is well known that the high hardness ceramic deforms and erodes de penetrator through a complex brittle fracture mechanism of the ceramic. The deformation process of the backing plate absorbs about 20-40% of the total kinetic energy of the projectile. The rest of the kinetic energy is spent to deform the projectile (10-15%) and a vast amount is

taken by the ejected ceramic debris [39]. The phenolic liner provides spall and fire protection. The whole system is cover by a fibre glass composite required to protect the ceramic tiles from low velocity impacts, arising from everyday normal vehicle operations.

2.2 Material testing

2.2.1 Basic concepts

For the purpose of this study, only the metallic alloys will be analysed, since only an aluminium alloy and a steel will be available for testing. But before proceeding to examine the tests conducted for these materials, a few concepts must be understood.

The most common relationship used in material characterization is the stress – strain. As Hanzell [18] explains, stress is a measure of the applied force, in Newtons (N), divided by the area over which that force acts, in square meters (m^2). The SI units therefore become N/m^2 or pascals (Pa).

In the case of simple tension, the stress, σ, can be written as,

$$\sigma = \frac{F}{A_R} \tag{1}$$

where F is the applied force, and A_R is the area over which the force acts. In a situation where the force no longer acts normal to the surface but as some angle to it, the component of the force acting parallel to the surface, Fs, loads the element in shear. So, a shear stress, τ, that is acting on the element can be defined as,

$$\tau = \frac{F_S}{A_R} \tag{2}$$

The states of stress can be categorized in three states of pure stress. They are defined as simple tension or compression (Eq. 1), pure shear (Eq. 2) and hydrostatic stress or pressure. This occurs when a solid is subjected to equal compression on all sides and is usually associated with shock waves in penetration and blasts. However, for the current work, we will focus mainly on simple tension.

A material will react to stress by deforming or straining. In the case of simple tension, then the amount of strain can be determined by measuring the amount of deformation and dividing it by the original length of the sample. So, strain, in simple tension, where a load is applied to a sample of length x_0 can be defined as,

$$\varepsilon_n = \frac{x - x_0}{x_0} \tag{3}$$

where x is the current length due to the application of the load. This is the definition of engineering or nominal strain where the initial and final states of the sample are measured during an experiment. However, there is an additional important definition of strain that is frequently used in computational codes, or in the analysis of wave propagation, designated true

strain or natural strain. For a continually straining object, it is the precise measure of strain at one particular point in time. Therefore, an increment of true strain can be defined according to,

$$d\varepsilon = \frac{dx}{x} \tag{4}$$

Integrating between x_0 and x, we have,

$$\varepsilon = \int_{x_0}^{x} \frac{dx}{x} = \ln(\frac{x}{x_0}) \tag{5}$$

From Eq. (3), it is seen that,

$$x = x_0(1 + \varepsilon_n) \tag{6}$$

Therefore, the equation for true strain can be rewritten as:

$$\varepsilon = \ln(\frac{x_0(1+\varepsilon_n)}{x_0}) \tag{7}$$

And so, true strain is defined as,

$$\varepsilon = \ln(1 + \varepsilon_n) \tag{8}$$

This gives us the relationship between true strain and engineering strain.

In simple tension, the length of the sample will increase, but the thickness, or diameter for cylindrical specimens, will decrease. To describe this effect, the Poisson's ratio (υ) relates the longitudinal strain to the transverse strain, ε_t; through,

$$\upsilon = -\frac{\varepsilon_t}{\varepsilon_n} \tag{9}$$

2.2.2 Elasticity

When a load is applied to a material, initially, it will deform elastically. In fact, all materials will deform elastically when subjected to small strains. Up to a predetermined stress limit, the amount of deformation is reversible as the material has not suffered permanent deformation. In this region, the stress is directly proportional to the strain; thus,

$$\sigma = E\varepsilon \tag{10}$$

where E is defined as the modulus of elasticity or the Young's modulus of the material. This relationship was originally discovered by Robert Hooke in 1878 and is sometimes referred to as *Hooke's law*. At the atomic level, ε is a measure of the increase in atomic spacing to the applied stress. As the load is increased, the inter-atomic spacing increases, and when the load is removed, the atoms return to their equilibrium position. The greater the attraction between atoms, that is, the stronger the bonding, the greater the stress required to increase the inter-atomic spacing.

2.2.3 Strength

The measurement of the strength of metal materials is generally carried out in tension by what is called a 'simple tensile test'. Loading a ductile material such as mild steel in a simple tension results in a stress-strain profile shown in Fig. 3. Inset is a typical 'dumbbell'-shaped specimen that may be used with metals showing a reduced section where the strain is measured. The curves for both true stress and engineering stress are shown. Considering the engineering stress behaviour: At point A, the yield strength (Y) of the material is reached. At this point, the material is no longer linear elastic and starts to incur permanent damage. This continues until at point B, the maximum engineering stress is reached, which is known as the ultimate tensile stress. At this point, the onset of necking occurs, and the stress is relaxed until fracture occurs at point C.

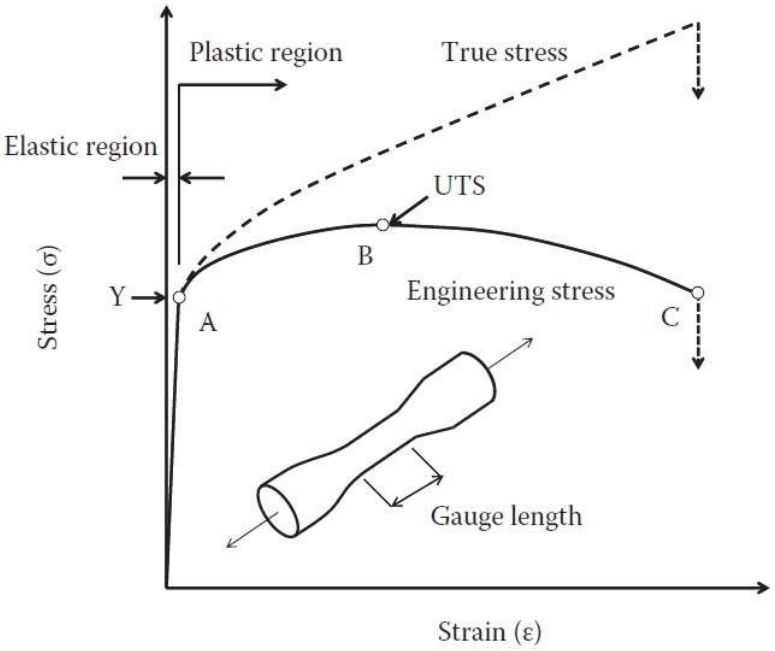

Figure 3: A schematic of a typical stress-strain curve for steel [18].

The engineering stress curve sits lower than the true stress curve. This is because the calculation of the engineering stress takes into account the original cross-sectional area before the sample is deformed. As the sample is stretched, it will narrow, and the true stress takes into account the reduced cross-sectional area, i.e. the instantaneous cross-sectional area.

The true stress and engineering stress are related by the following relationship:

$$\sigma = \sigma_n(1 + \varepsilon_n) \tag{11}$$

Where σ_n is the engineering stress, and ε_n is the engineering strain.

The application of tensile load produces strains in the test specimens. The effect of these strains is to rise the energy levels in the bar itself. The increase in energy within the bar is

called *strain energy* and is equal to the work done on the bar provided that no energy is added or subtracted in the form of heat. The strain energy, U, can be calculated from,

$$U = F.dx \tag{12}$$

Where F is the load applied to the bar, and x is the distance through which the bar is stretched. The above equation including the cross-sectional area A and the original length L of the bar can be rewritten as follows:

$$U = A_R.L.\frac{F}{A_R}.\frac{dx}{L} \tag{13}$$

And therefore,

$$\frac{U}{W} = \sigma.d\varepsilon \tag{14}$$

Consequently, the area under the curve is a measure of the strain energy per volume unit, W, and is a measure of the material's toughness.

2.2.4 Strain measurement

The measurement of the strain during testing is fundamental for the correct estimation of the material behaviour. However, there are several difficulties associated with the acquisition of this data. If the deformations beyond the maximum engineering stress are of little relevance for the application intended, the simple use of an extensometer, or a strain gauge measuring the deformation on the specimens' reduced section is sufficient. But, if precise strains are required after the maximum engineering strain is achieved, these methods will not be enough, due to the unset of localized necking.

For strain measurements, up until fracture occurs, video or laser extensometry is usually applied. These methods rely on analysing the deformations from the specimens' entire surface allowing for the determination of the strains on the necking region. With round test bars, the instant diameter, and thus instant true cross-sectional area, can be easily tracked. But, more often than not, the only available material for testing is fabricated from flat sheets or plates, resulting in a rectangular cross section. Strain measurement on these specimens becomes complicated due to inhomogeneous strain field and triaxial stress. Two practical difficulties can be mentioned here. The first problem is the measurement of the instantaneous area of minimum cross-section after necking. During plastic instability, the cross-section at the largest deformed zone forms a cushion like shape [40], so that it becomes difficult to measure the cross-sectional area of the neck. The second challenge is the measurement of thickness reduction. Some commercially available solutions offer a two-camera system positioned symmetrically oblique to the specimens' surface, allowing for instant tracking the thickness reduction. Afterwards, the images obtained are compared through a Digital Image Correlation (DIC) software that will analyse the variance between both cameras and between each frame permitting the tracking of the true cross-sectional area and necking strains throughout a test.

These commercial systems tend to be very expensive, limiting their availability to more well-funded laboratories. It is, however, possible to create a home integrated system using a modern digital camera and an open source DIC software to obtain similar results, as Geesthacht et al. [40] and Ahmmad et al. [41] demonstrate. This method relies on a single digital camera to measure the strain field on the specimen surface allowing for the estimation of a/R, where a is the half-thickness and R is the radius curvature of the neck surface (Fig 7a).

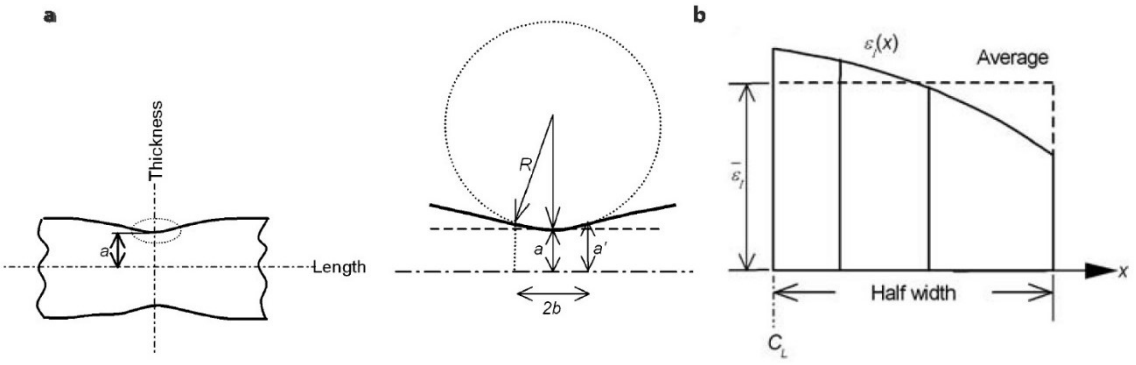

Figure 4: a) Illustration of neck geometry, a half-thickness of the neck, a' half-thickness at location b, R radius of curvature of the surface at the neck. b) Estimation of average axial strain ($\bar{\varepsilon}_x$). C_L centre line [44].

The processes for determining the true stress and true strain with this method begins with the effective strain, $\bar{\varepsilon}$, after bifurcation as calculated by Scheider et al. [40] as:

$$\bar{\varepsilon} = \sqrt{\frac{4}{3}\left(\varepsilon_x^2 + \varepsilon_x\varepsilon_y + \varepsilon_y^2\right)} \tag{15}$$

where ε_x and ε_y are the true strains in the specimen's length and width directions, respectively. Usually necking phenomena occur soon after the maximum load, and the initiation of necking, true stress can be calculated by:

$$\sigma = \frac{F}{A_R} = \frac{F}{A_0} exp\left(-\varepsilon_y - \varepsilon_z\right) \tag{16}$$

where A_0 is the specimen's initial cross-sectional area and ε_z is the strain in the thickness direction. In the case where deformation is uniform, Eq. (16) can be calculated as:

$$\sigma = \frac{F}{A_0} exp(\varepsilon_x) \tag{17}$$

In practice, the axial strain over the cross-section, as shown in Fig 4a, is not uniform, so that an average true stress (σ_T) can be obtained from Eq. (17) by measuring an average axial strain, $\bar{\varepsilon}_l$ (see fig 4b):

$$\sigma_T = \frac{F}{A_0} exp(\bar{\varepsilon}_x) \tag{18}$$

The true equivalent stress, σ_{eq}, after correction due to the triaxial stress state, can be expressed as:

$$\sigma_{eq} = \frac{\sigma_T}{C_B} \text{ or } \frac{\sigma_T}{C_O} \tag{19}$$

where C_B and C_O are two analytical correction factors that can be used for rectangular cross-section specimens after the initiation of necking. These factors are given by Bridgman [42]:

$$C_B = \left[\left(1+\frac{2R}{a}\right)^{1/2} ln\left\{1+\frac{a}{R}+\left(\frac{2a}{R}\right)^{1/2}\left(1+\frac{a}{2R}\right)^{1/2}\right\}-1\right] \tag{20}$$

and by Ostsemin [43]:

$$C_O = \left(1+\frac{a}{5R}\right) \tag{21}$$

where a and R are defined as illustrated in Fig 4a, in which the solid bold line represents the upper surface of the central line section of the neck. The correction factors C_B and C_O depend on a parameter, a/R, given by:

$$\frac{a}{R} = \frac{2a(a'-a)}{(a'-a)^2+b^2} \tag{22}$$

where a/b may be taken as $0.5-1.0$ [44], and the half-thickness, a', is estimated at a distance b from the centre of the neck (see Fig 4a). The continuous values of the thickness can be estimated by surface strains in the length and width directions by a vision sensor by applying the following relations:

$$a = a_0 exp(\varepsilon_z) = a_0 exp\left(-\varepsilon_x - \varepsilon_y\right) \tag{23}$$

$$a' = a_0 exp(\varepsilon'_z) = a_0 exp\left(-\varepsilon'_x - \varepsilon'_y\right) \tag{24}$$

where a_0 is the initial value of the half-thickness.

2.2.5 Dynamic behaviour of materials

Simple tensile tests, however, can not completely describe the full material behaviour, for example, when a bullet, penetrator or shaped charge jet impacts and perforates a material, the rate of deformation the projectile encounters is much higher than what is observed in conventional quasi-static material tests. The behaviour of the metal (projectile) and the armour target is different at high rates of loading than at relatively small loading rates. There are various tests that can be used to assess behaviour and measure properties. Fig. 5 summarises the range of strain rates that are of interest to material scientists and engineers. As the strain rates are increased, it is necessary to use different techniques to probe the response of the material and to measure the state of stress under dynamic loading.

For materials that are subjected to relatively high strain rates (when compared to quasi-static values), their strengths can be changed and, for most materials, noticeably increase. Generally speaking, metals will get stronger but less ductile at elevated strain rates, but unlike some non-metals, their stiffness is relatively unaffected by increase deformation rates.

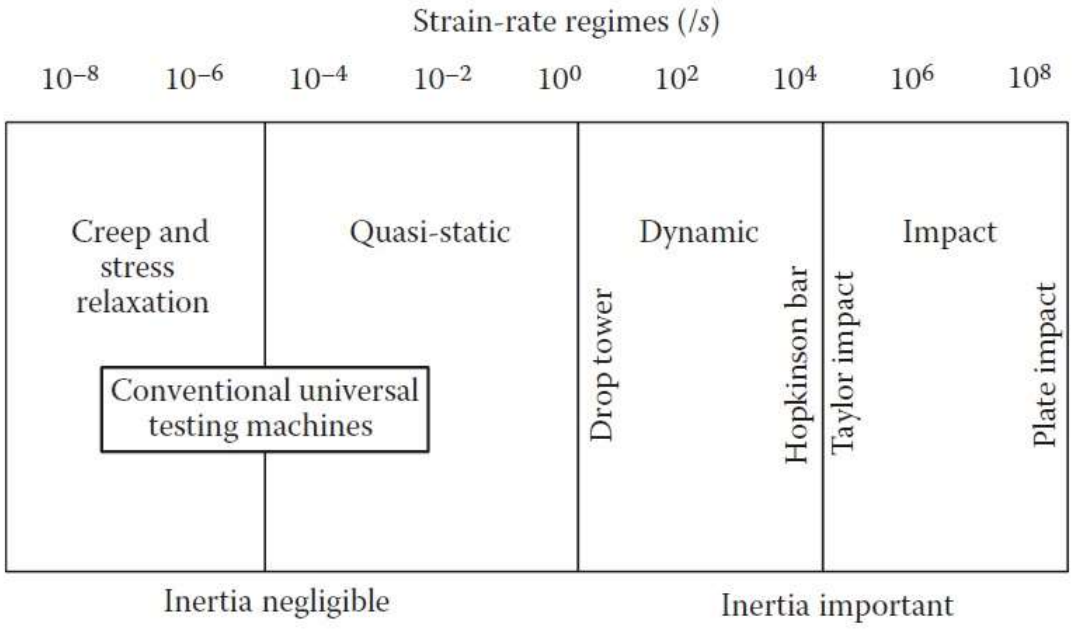

Figure 5: Strain-rate regimes [38].

The reason for the increased strength with strain rate is due to complex micro-structural behaviour that is dependent on the nature of the material. For example, with most metals, the mechanism can be explained by dislocation movements being impeded during plastic deformation. For most metals, it is generally recognised that the dynamic yield strength of a material (or flow stress) can be defined by the following proportionality [18]:

$$\sigma \propto \ln \dot{\varepsilon} \tag{25}$$

where $\dot{\varepsilon}$ is the strain rate; it has units of s^{-1}. The flow stress in this case is the stress taken at any point along the plastic stress-strain curve.

2.2.6 Material constitutive models

Through computational codes designated hydrocodes, one can simulate dynamic phenomena such as impact and penetration using constitutional models that are able to describe the tensile flow stress of the material. One of the most widely used equations was given by Johnson and Cook (J-C) [45]. The equation is given by:

$$\sigma_Y = \left(A + B\varepsilon_p^n\right)(1 + C \ln \dot{\varepsilon}_p^*)(1 - T_H^m) \tag{26}$$

where A is the yield strength of the material, B the strain hardening constant, ε_p the amount of plastic strain, n the strain (or work) hardening exponent, C a strain-rate constant, $\dot{\varepsilon}_p^*$ the dimensionless plastic strain rate for $\dot{\varepsilon}_0$ (quasi-static tensile test strain rate), m the thermal softening exponent and T_H the homologous temperature $\{T_H = (T - T_r)/(T_m - T_r)\}$,where T is the absolute temperature, T_r is the room temperature and T_m is the material's melting temperature. The first set of brackets gives the strain hardening term and can be determined by simple tensile tests. The second set represents the strain rate hardening behaviour and requires analysing the same point along the plastic stress-strain curve on multiple strain rates. Finally, the third set represents the thermal softening. This is a phenomenon generated by the considerable amount of work converted into heat during inelastic deformation. This leads to a reduction on the materials flow strength with increasing temperature. For high strain-rate applications, the process is adiabatic as there is little time for heat to be dissipated in the surrounding material.

However, this equation does not describe fracture. Johnson and Cook also proposed a model including the effects of stress triaxiality, temperature, strain rate on failure strain. The Johnson-Cook damage model is a cumulative damage-fracture model that takes into account the loading history, which is represented by the strain to fracture (ε^f). In other words, model assumes that damage accumulates in the material during the plastic straining ($\Delta\varepsilon$) and the material breaks immediately when the damage reaches a critical value. This means the damage has no contribution on the stress field until the fracture happens. J-C is an instantaneous failure model, which means no strength remains after erosion of an element. The damage of an element is defined on a cumulative damage law:

$$D = \sum \frac{\Delta\varepsilon}{\varepsilon^f} \tag{27}$$

In which

$$\varepsilon^f = \left(D_1 + D_2 EXP(D_3\sigma^*)\right)\left(1 + D_4 \ln\left|\dot{\varepsilon}_p^*\right|\right)(1 + D_5 T_H) \tag{28}$$

where D_{1-5} are the J-C cumulative damage model parameters and the dimensionless pressure/stress ratio (σ^* is the ratio of hydrostatic stress σ_H per effective stress σ_{eff}) is a measure of triaxiality of the state and defined as:

$$\sigma^* = \frac{\sigma_H}{\sigma_{eff}} = \frac{(\sigma_x+\sigma_y+\sigma_z)/3}{\sqrt{\sigma_x^2+\sigma_y^2+\sigma_z^2-\sigma_x\sigma_y-\sigma_y\sigma_z-\sigma_z\sigma_x+3\left(\tau_{xy}^2\tau_{yz}^2\tau_{zx}^2\right)}} \tag{29}$$

where, σ_x σ_y σ_z are the stresses in the length, with and thickness directions respectively and τ_{xy} τ_{yz} τ_{zx} are the shear stresses between the length and width, with and thickness and thickness and length directions respectively. The damage variable D takes values between 0 and 1, where $D = 0$ for an undamaged material and the failure of the elements assumed to occur when $D = 1$. The failure strain and thus the accumulation of damage is a function of mean stress, strain rate and temperature [46].

Cockcroft-Latham (C-L) suggested another fracture criterion [47] based on the strain energy per volume unit W. This criterion is expressed as,

$$W = \int_0^{\varepsilon_{eq}} \langle \sigma_1 \rangle d\varepsilon_{eq} \leq W_{cr} \tag{30}$$

where W_{cr} is the critical value of W which is represented by the area under the stress-strain curve and, unlike the J-C failure criterion, can be determined from simple uniaxial tensile tests, σ_1 is the major principal stress, and $\langle \quad \rangle$ is the Macauley bracket which can be defined as:

$$\langle S \rangle = \begin{cases} S \; if \; S > 0 \\ 0 \; if \; S \leq 0 \end{cases} \tag{31}$$

This model however, is based on only one constant to indicate the fracture properties of a material and does not take into account the materials change in response to different strain rates for example, making it a very limited model. Nevertheless, Flores-Johnson et al [23] successfully used it, in addition to a deletion criterion for when the element temperature equals 90% of the melting temperature, to simulate ballistic impacts in various metal alloys obtaining acceptable result for preliminary analysis.

There are several more constitutive models and failure constitutive models available in commercial hydrocodes, however for this work, due to limitations in time and testing equipment, we will establish the objective of determining the strain hardening constants for the strain hardening constants for the J-C constitutive model and the C-L failure criterion.

3 Experimental Methodology

For this project, a 5 mm and 10 mm thick aluminium AW-5083-H111 and a 2.2 mm thick Ramor 500 steel alloys will be subjected to tensile testing at a quasi-static strain rate for the purpose of mechanical characterization. These alloys are known for their good behaviour under ballistic impacts and have already been used in effective armour products [18]. Five specimens from three rolling directions, 0º, 45º and 90º, and every thickness were produced to make for a total of 45 specimens. The current chapter will describe the fabrication and preparation method, the experimental equipment and the experimental procedure followed in order to mechanically characterise these alloys.

3.1 Fabrication Method

The selection of the material fell under the responsibility of *CEiiA*, the project coordinator. *Ramor 500* 2.2mm thick from *SSAB* was the steel of choice, and the *AW-5083-H111*, 5 mm and 10 mm thick was the aluminium acquired. The chemical composition of both can be found in Table 1 and 2, and in Table 3 their respective generic physical and mechanical properties.8

Table 1: Chemical composition of Ramor 500 (max %) [48].

C	Si	Mn	P	S	Cr	Ni	Mo	B
0.35	0.70	1.50	0.015	0.010	1.0	2.0	0.70	0.005

Table 2: Chemical composition of AW-5083-H111 (%) [49].

Si	Fe	Cu	Mn	Mg	Cr	Zn	Ti	Other (each)	Other (total)
0.4	0.4	0.1	0.4 – 1.0	4.0 – 4.9	0.05 – 0.25	0.10	0.05 – 0.25	0.0 – 0.05	0.0 – 0.015

Table 3: Generic physical and mechanical properties of Aw-5083-H111 and Ramor 500.

	Density (g/cm^3)	Melting Point (C)	Modulus of Elasticity (GPa)	Proof Stress (MPa)	Tensile Strength (MPa)	Hardness Brinell (HB)
AW-5083-H111 [49] (0.2-6.3mm)	2.65	570	72	125 min.	275-350	75
AW-5083-H111 [49] (6.3-80mm)	2.65	570	72	115 min	270-345	75
Ramor 500 [50]	7.50*	717*	198*	1450	1700	480-560

* average values for high carbon content steels from [51].

The alloys were only available in flat sheets, and for this reason, the specimens were constrained to rectangular cross sections. Their fabrication also was the responsibility of *CEiiA*. The specimens' dimensions and testing followed the guide lines proposed by the *American Society for Testing and Materials (ASTM) E 8M* standard [52] and the dimensions of the manufactured specimens are displayed in Fig. 6. Five specimens were produced for each

thickness and for each of the three directions relative to rolling (0º, 45º and 90º) bringing the total number of specimens to 45, being the adopted designation presented in Table 4.

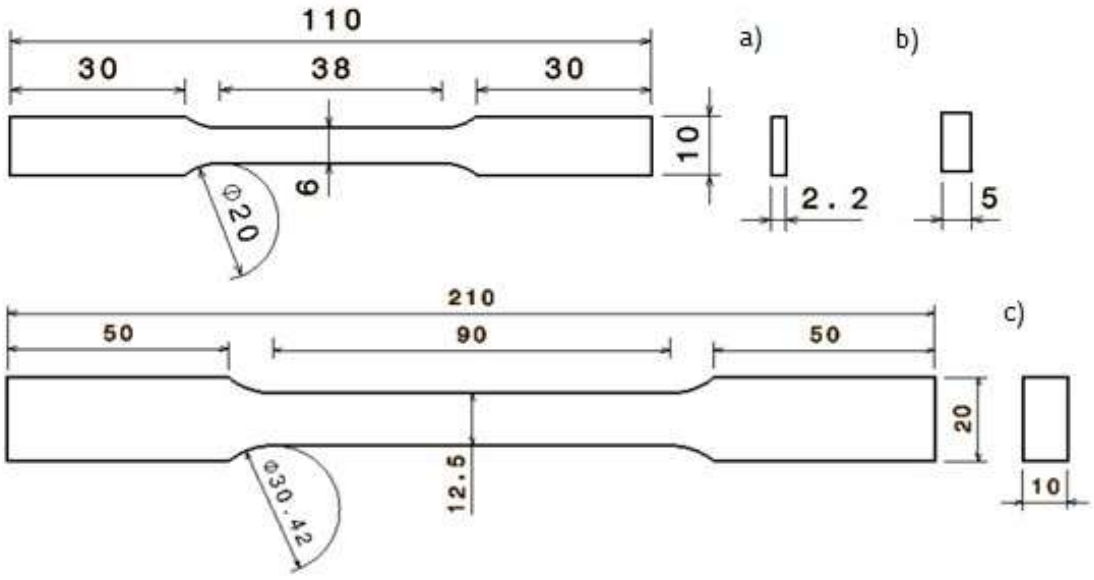

Figure 6: Dimensions of the manufactured specimens, a) Ramor 500 2.2 mm, b) and c) AW-5083 of 5 mm and 10 mm thickness respectively.

Table 4: Example of the designation of a specimen and respective meaning.

AlN1045B

Material	Specimens size	Specimens dimensions	Cutting direction	Specimens designation
Al – Aluminium St – Steel	S – reduced size N – standard size	2.2 - 2.2 mm 5 – 5 mm 10 – 10 mm	00 – with the rolling direction 45 – oblique to the rolling direction 90 – perpendicular to the rolling direction	A, B, C, D or E

Before testing could proceed, some preparations were carried out on the specimens in order to equip them for mechanical testing. The first step was the application of the strain gauges to the face of the specimen. These strain gauges will ensure that the DIC measurements are accurate, provide better readings for low strain deformations and more precise Poisson's ratio measurements. The application of the strain gauges followed the instructions contained in their manual guide lines. The overall process is represented in Fig. 7. First the surface of the specimens was polished with sandpaper, grade #320 for the steel and #600 for the aluminium, until the surface was flat and smooth without any oxidation (Fig. 7b). Afterwards the bonding surface was cleaned by wiping it along a single direction with industrial tissue damped with acetone, and the strain gauge guide lines were scribed on the bonding area using a 4H pencil.

The strain gauges were then applied after adding a small amount of CC-36 adhesive on the back of the gauge and pressing them with the thumb through a polyethylene sheet inside the scribed guides. After pressing during the recommended time, the bond was checked to ensure proper adhesion to the surface (Fig. 7c). Finally, a layer of coating was applied to protect the strain gauge from the environment (Fig. 7d).

Once the strain gauges were applied, the surface treatment for the DIC could be initiated. The procedure began by surface polishing with sandpaper, grade #320 for the steel and #600 for the aluminium, as with the strain gauges (Fig. 7f). Secondly the polished surface was degreased with an acetone soaked industrial paper, unidirectionally scrubbing the specimens' surface. Next, three layers of base white paint were applied on the clean surface (Fig. 7g). A high temperature AT 800 white paint with fast drying speed was used. This paint was chosen due to its high adherence and high strain resistance since normal spray suffered adherence problems on calibration tests. After letting the base paint dry, the stochastic patterns were generated by applying a light spray of black paint on top of the base (Fig. 7h). This time the paint was a normal acrylic based paint because it did not suffer from adhesion problems due to the small area of the dots.

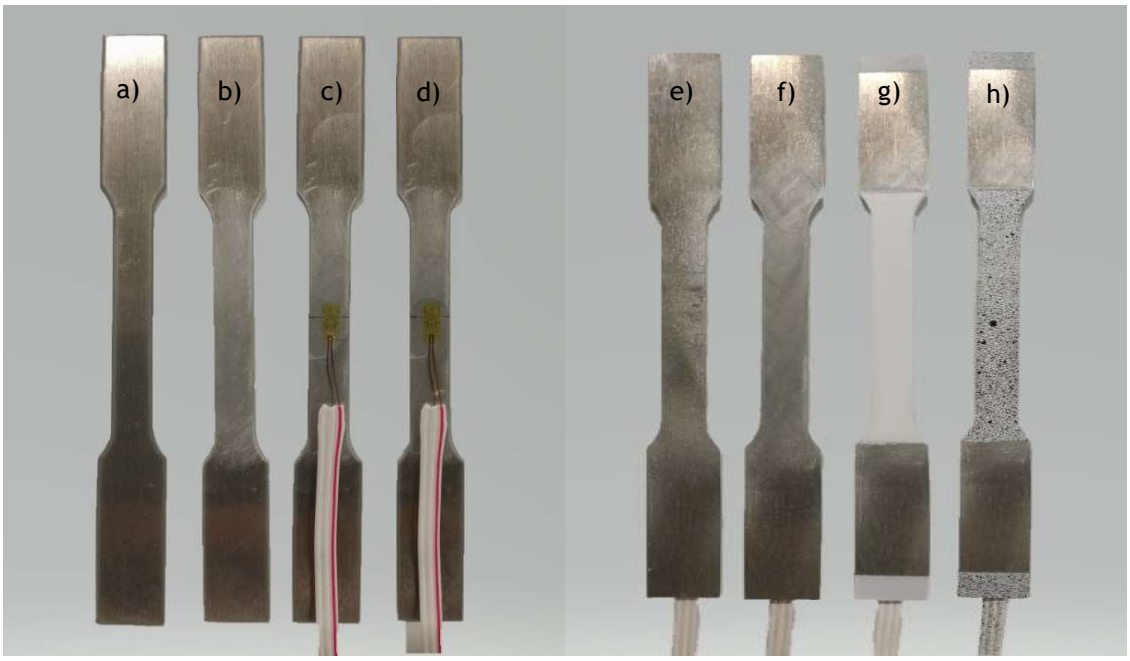

Figure 7: Stages of preparation of a specimen; a) untreated surface, b) clean surface, c) applied strain gauge, d) protective coating, e) untreated back surface, f) clean back surface, g) base white paint and h) stochastic pattern.

3.2 Equipment

The tests for the steel and the 5 mm thick aluminium were carried out in a universal testing machine *SHIMADZU AG-IC* (Fig. 8a), installed in the Vibrations and Structures Laboratory of Universidade da Beira Interior. This equipment has a load cell type *SFL-50KNAG* with a limit

load of 50 kN and its control was performed by the manufacturer supplied software, *TRAPEZIUMX V1.3.0*. Through this software, the test method is defined by selecting the test mode, units, velocity of head separation, specimen dimensions and frequency of the data acquisition.

For the 10 mm thick aluminium, an *INSTRON 1341* servo hydraulic universal testing machine (Fig. 8b), on the Materials Laboratory of Universidade da Beira Interior, equipped with a *2518-111100kN* D load cell was used instead, due to the *SHIMADZU* physical limitations. The software controlling the machine was the manufacturer provided WaveMatrix V1.5. The remaining procedure was unchanged.

Figure 8: a) *SHIMADZU AG-IC*; b) *INSTRON 1341*.

For a mechanical strain measurement, accurate low strain measurements and corroboration of the DIC measured data, *KFEM-1-120-C1L3M3R* and *KFG-1-120-D16-11L3M3S* strain gauges from *KYOWA*, were applied to the specimens surface. The strain gauges were applied with *CC-36* adhesive and the application procedure followed *KYOWA*'s manual as described in 3.1. The strain gauges were connected to a *National Instruments TB 4330* 8 channel bridge input, connected to a *National Instruments PXIe-1073 chassis* in order to digitize the analogical strain gauges signal. The connections were implemented as indicated by the terminal block's manual, and the digital data obtained was then analysed and extracted to *EXCEL* by the systems engineering software *LabVIEW 2014 V14.0f1 (32 bits)*. The block diagram and front panel generated for these tests are available in Appendix A.

The DIC system was home integrated due to the high cost of commercial solutions. The equipment used for it was a *NIKON D3300* camera with a resolution of 24.2 megapixels, a tripod,

a simple light source and the stochastic patterns on the specimens' surface. After the execution of the tests the images obtained were analysed in *GOM Correlate* V2.0.1 software. The GOM Correlate software is based on a parametric concept, which forms the underlying foundation for every single function. With the parametric concept, each individual element retains its creation path within the software structure. All actions and evaluation steps are fully traceable and interlinked. Individual elements can be modified and adjusted at any time, and a one-button solution updates all dependent elements automatically after changes have been made. This parametric approach ensures that all process steps are traceable, thus guaranteeing process reliability for measuring results and reports. [53]

3.3 Experimental Procedure

After the specimens were treated and dried, and the software tested, the tests were performed as follows.

Figure 9: Experimental Setup in the SHIMADZU AG-IC.

First the testing machine software was set running, one end of a specimen was clamped to the testing machines' top clamp, and then lowered to the testing position. Secondly the Strain gages were connected to the *National Instruments PXIe-1073 chassis,* and then turned on as well as the computer to which it was connected. Before clamping the lower clamp, the machine and strain gauges were software calibrated. The errors associated with the clamping procedure would only be subtracted to the final results, after the test was conducted. After clamping the

lower end of the specimen, the prepositioned tripod and camera were readjusted so that the camera would face the specimen perpendicularly. Having the camera and lighting turned on the *LabVIEW* program was set running and the camera started recording. When the counter on the program went to zero and some readings appeared on the display, the test was started in the *TRAPEZIUMX*. The full experimental setup can be seen in Fig. 9.

The test would then resume till the specimens' failure occurred and the machines' software automatically stopped. The camera and *LabVIEW* program were manually stopped, the room temperature noted and the data from all sources was retrieved. The chassis computer and the chassis were shut down and the strain gauges disconnected. Lastly, the two pieces of the fractured specimen were unclamped, removed and the dimensions taken with a calliper. the next specimen was, then, readied for testing and the procedure reinitiated.

4 Results and Discussion

4.1 AW-5083-H111 Results

4.1.1 5 mm Thick Specimens

After having conducted the tensile tests, it was now necessary to process and analyse de data obtained from the different sources.

This process began by synchronizing the data from the strain gauges and the universal testing machine. This was achieved by matching key points on the load-time graph with the time-strain graph. The stress-strain curves were constructed, and the Youngs' Modulus and the yield point at 0.2% were determined as represented in Fig. 10.

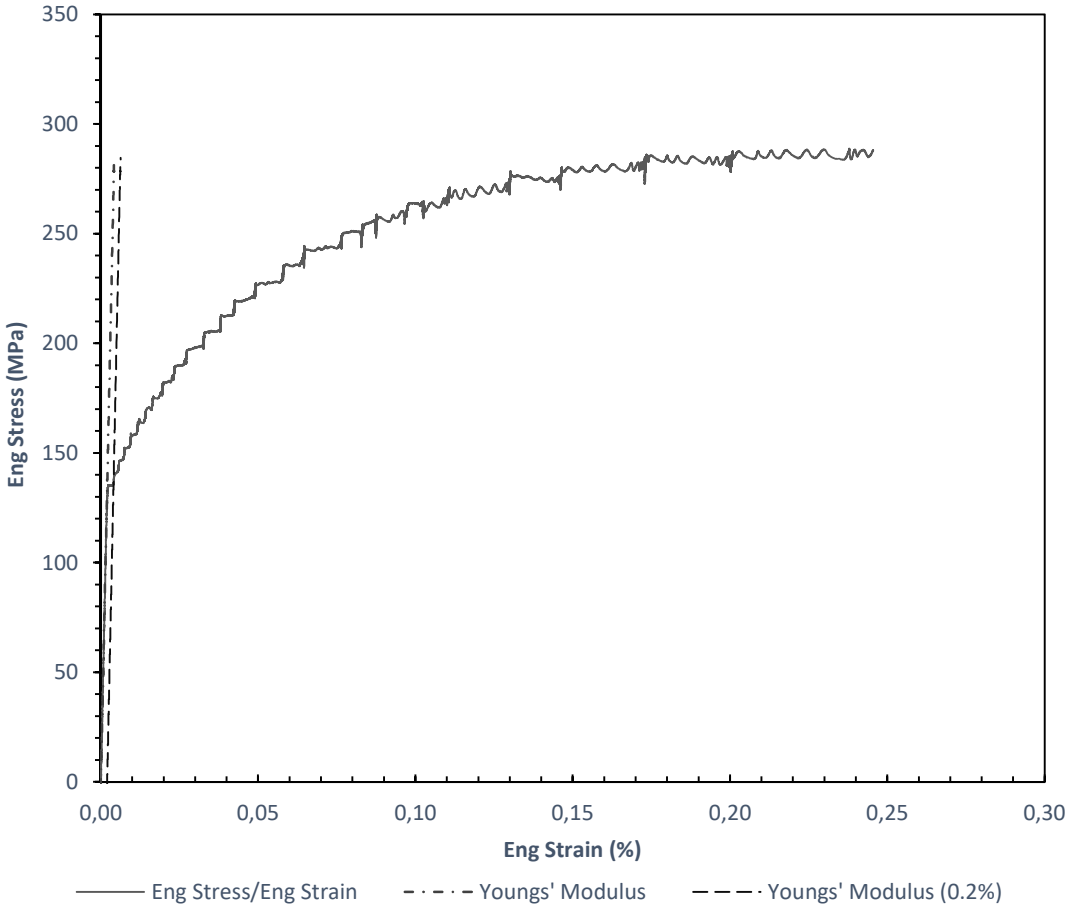

Figure 10: Engineering stress-strain curve for AlS500A, as well as the Youngs' Modulus and Youngs' Modulus at 0.2%.

Two phenomena immediately become clear in Fig. 10, consisting of both "serrations" and instabilities of high frequency oscillations in the plastic deformation region. These phenomena are present in every test from this aluminium. As Motsi et al. explain [54], the applied strain rate has an effect on the mechanical properties with regard to the dynamic strain aging (DSA).

This causes aluminium alloy 5083 to be insensitive or, rather, to exhibit a negative strain rate sensitivity. Crystal defects exist in the material and these include substitution of matrix atoms by alloying elements with similar radius and also, the misalignment of atoms in the crystal lattice known as dislocations. In this alloy the major alloying element is Magnesium (Mg) which is very mobile. When an external stress is applied to the material, dislocations move and get temporarily arrested by obstacles [55], this characterizes the DSA phenomenon observed in the tests. During this period, the Mg atoms diffuse around the dislocation cores and remain there. Additionally, there is a formation of instabilities of high-frequency oscillations in the plastic deformation region designated as 'serrated' or 'jerky' flow [56]. These serrations are formed by a combined effect of Mg atoms migration, slip bands propagation deformation, micro-void nucleation growth and coalescence [57].

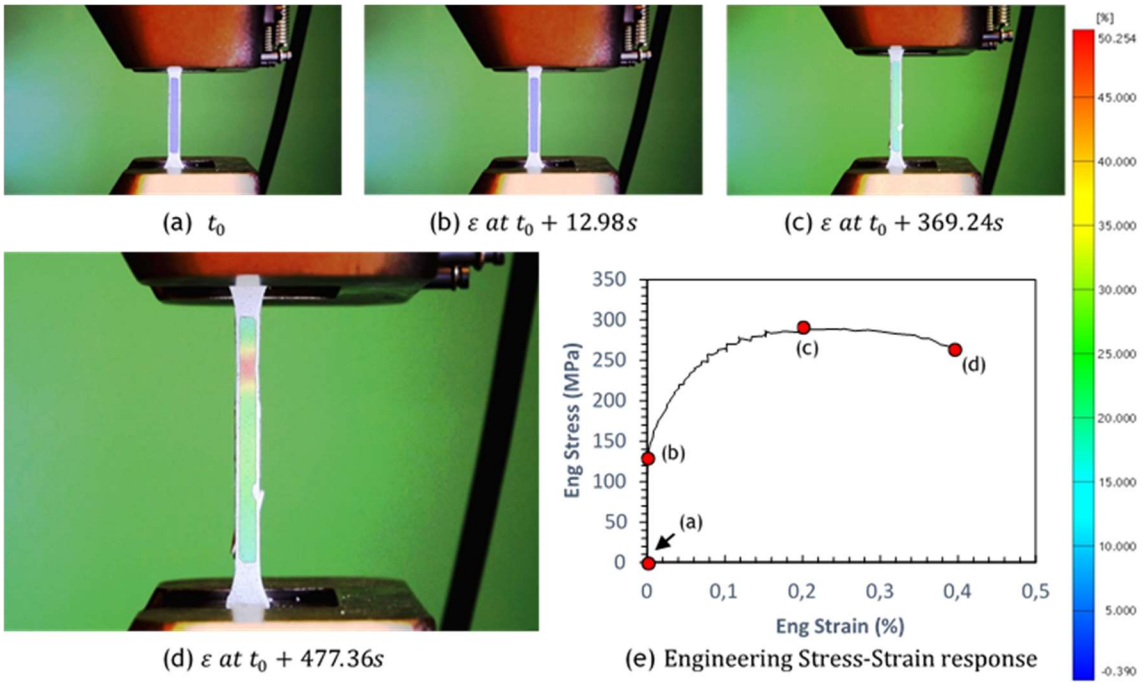

Figure 11: GOM analysis of the AlS500A Specimen loading axis strain at initial time (a), 0.2% Yield (b), maximum force (c) and just prior to rupture (d). (e) is the obtained engineering stress-strain curve.

Due to the large deformation of the test subjects, the strain gauges were unable to reach engineering strains larger than 0.25 without becoming unglued and, taking into consideration that it is impossible to predict exactly where the necking region, and for that matter, fracture, will occur, without previously notching the testing subjects, it was, as aforementioned, necessary to use a digital image correlation (DIC) technic to get accurate measurements of the strain in the necking area. The data treatment followed the method described in section 2.2.4. In Fig. 11 the full evolution of the AlS500A specimen test, from initial time (a), to yield strength (b), maximum force (c) and just prior to fracture (d) is displayed. In (e) the full engineering stress-strain curve of the specimen is displayed. Up until the maximum force the strains are relatively homogenous across the specimen, for the exception of the previous described DSA phenomenon. Soon after maximum load is reached, necking starts to form accumulating

damage in that region exclusively. Though a full video recording of the tests took place, at the rate of 50 Hz, the memory and processing limits of the hardware available limited the strain analysis, from this method, to a frame for every 5 seconds of testing corresponding to a strain increment of $\Delta\varepsilon^0 = 2.5 \cdot 10^{-3}$, measured over a length of $L_0 = 51.5\,mm$. In addition, due to the very small strains and linear behaviour verified during elastic behaviour, it was chosen to ignore the frames leading up to the yield strength.

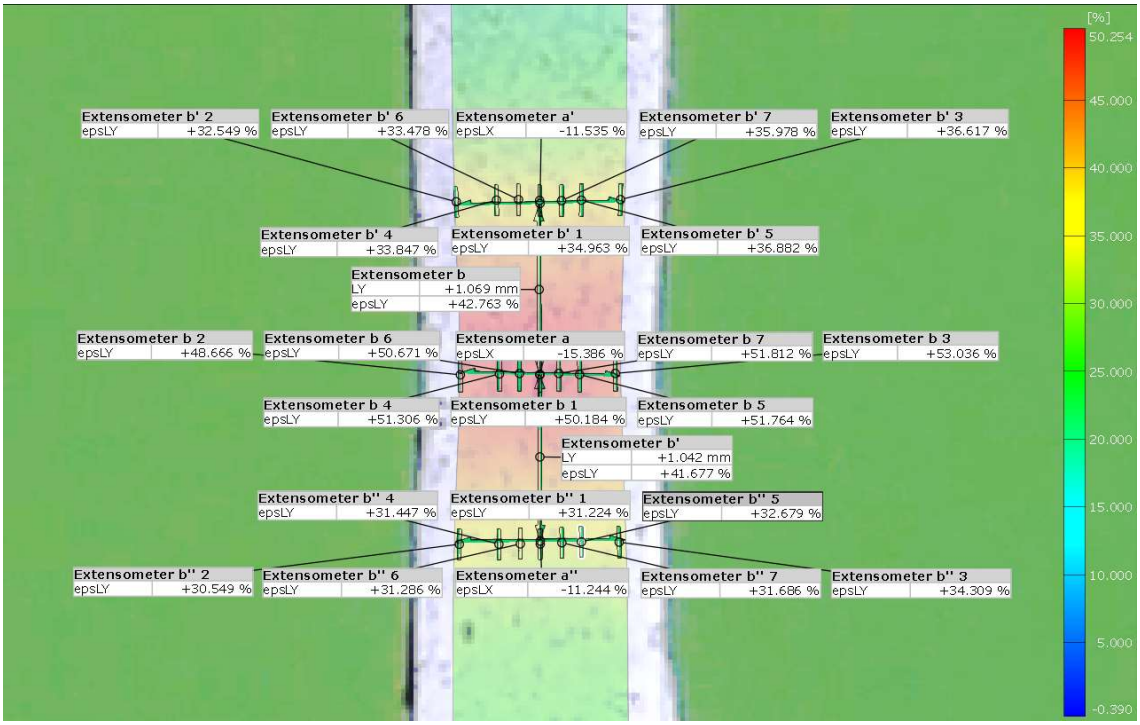

Figure 12: Scheme of virtual extensometers used in the AlS500A to estimate the average strain.

To be able to apply the Bridgman and Ostsemin corrections, it was necessary to determine a, a' and b from Eq. (22). This was achieved by creating virtual strain gauges on the specimens' surface and retrieving an average as explained in 2.2.4. The configuration observed in Fig. 12 was normally used, though, due to paint adherence problems, sometimes, only one side was able to be processed, and in some few cases, the data was unable to be retrieved.

Fig. 13 shows the true stress-strain curve from the strain gauge against the data from the DIC method. As we can see the correlation is very good, though, some discrepancies can be observed between the peaks from the serrations, possibly due to the different positioning of the strain gauge compared to the analysed area from the DIC. The low number of stages analysed does not allow the observation of the high-frequency oscillations. Also, the DSA behaviour has the interesting effect of causing irregular strain increases in different regions of the specimen, which leads to different strain serrations in different regions of the specimen, providing some justification to the deviations in the serration peaks between the measurements. For this reason, low strain data, such as yield strength and young's modulus are determined from the strain gauge data.

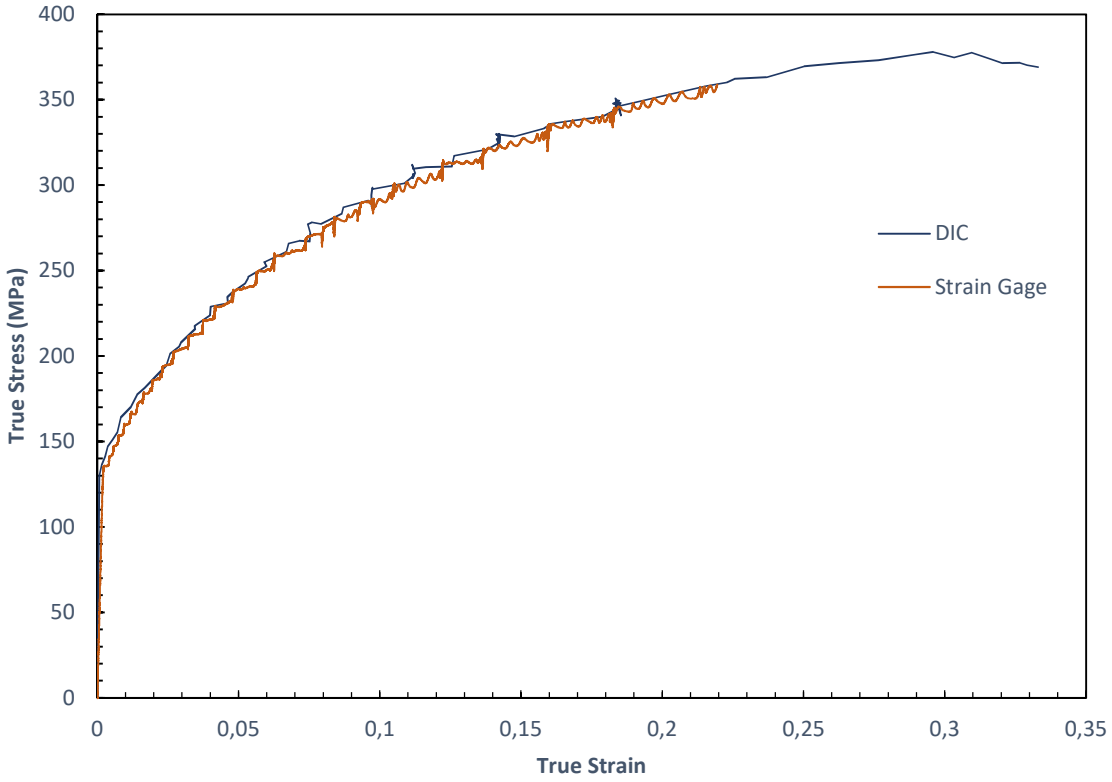

Figure 13: DIC obtained strains compared to strain gauge measurements of AlS500A.

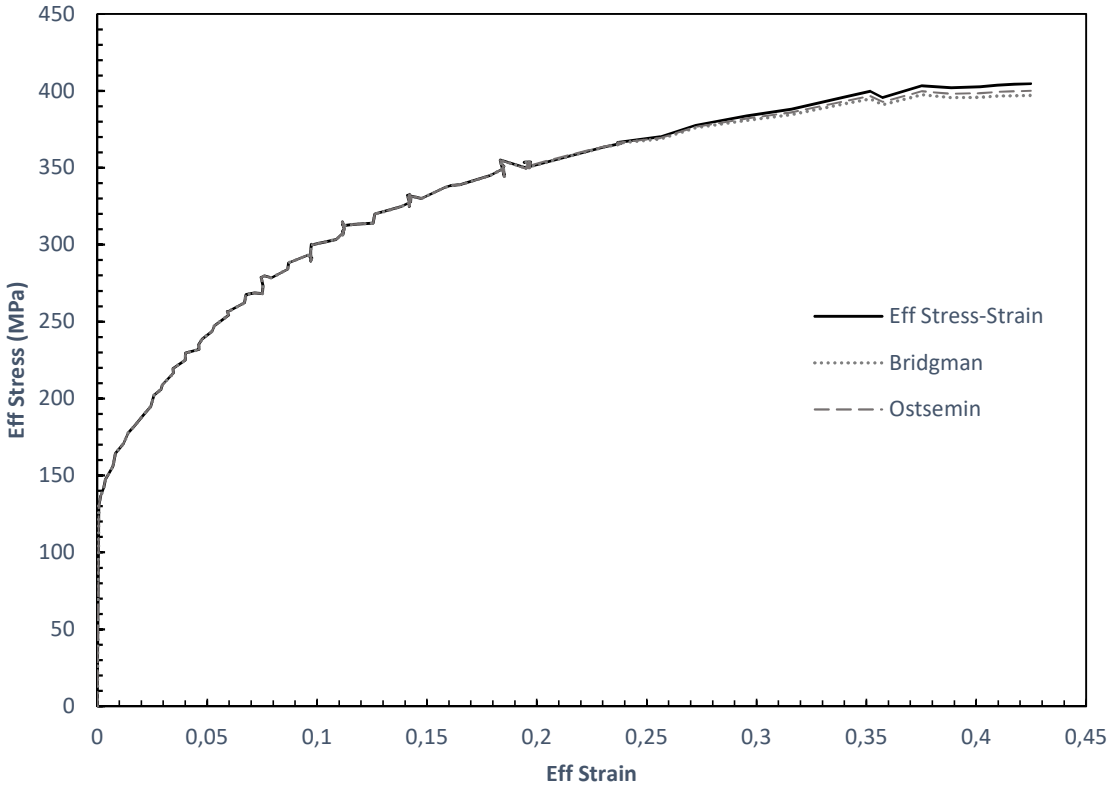

Figure 14:True stress-strain relationship of AlS500A; average true stress defined by Eq. (18), and the corrected equivalent stresses defined by Eq. (19).

Applying the procedure discussed in section 2.2.4, the effective stress-strain relationships are obtained and compared to the true stress-strain curve of the AlS500A as exemplified in Fig 14. Note that all the tests were processed using the Ostsemin correction.

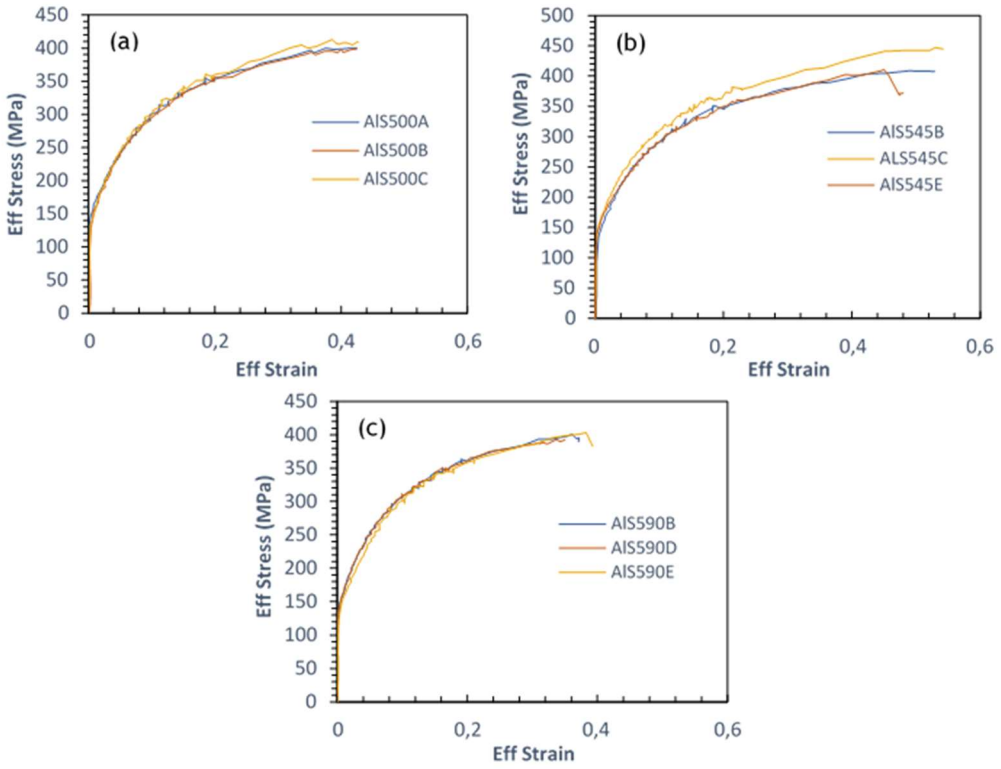

Figure 15: Corrected stress-strain curves from the 5 mm thick specimens; (a) 0º direction, (b) 45º direction and (c) 90º direction.

Table 5: Properties from the 5 mm thick specimens.

	Yield Strength 0.2% (MPa)	Tensile Strength (MPa)	E (GPa)	Poisson's Ratio	Elongation (%)	Failure Strain	W_{cr} (MPa)	Temp. (ºC)
AlS500A	136	400	67.2	-	27.22	0.42	142	17.3
AlS500B	134	398	67.5	-	24.80	0.42	140	17.8
AlS500C	137	408	68.8	-	26.28	0.43	145	17.8
Average	135	402	67.8	-	26.1	0.42	143	17.6
SD	1.41	4.32	0.70		1.00	0.006	2.16	0.24
AlS545B	139	408	66.5	-	24.2	0.53	182	19.3
AlS545C	141	445	66.5	-	28.77	0.54	201	19.3
AlS545E	135	372	66.3	-	24.46	0.48	163	19.1
Average	138	408	66.4	-	25.81	0.51	182	19.2
SD	2.52	29.80	0.1		2.10	0.03	15.51	0.1
AlS590B	138	391	66.5	-	23.77	0.37	124	19.2
AlS590D	143	392	66.7	-	24.24	0.35	115	19.6
AlS590E	138	385	65.5	-	23.79	0.39	130	19.9
Average	140	390	66.3	-	23.93	0.37	123	19.6
SD	2.38	3.16	0.53		0.22	0.02	6.16	0.29
Total Average	138	400	66.8	-	25.28	0.44	149	18.8

E: Young's modulus; W_{cr}: Work per volume unit; SD: Standard deviation.

The results obtained, and corrected, from the tests are compiled in the 3 different directions of study in Fig 15. As it is clear from the graphs, the 0º and 90º cutting directions exhibited remarkable invariance, despite the DSA effects. Both directions also exhibited approximate failure stress and strain values. As for the 45º direction, there were generally higher failure stresses and strains. The AlS545C had an unusual high stress resistance throughout the entire test and the failure strain was also relatively higher, though not so discrepant. Another interesting point comes from the observation that AlS545E decreased considerably the amount of stress supported just prior to rupture but without complete failure. This might indicate that the stresses and grain orientation originated from the fabrication process allow the material to tolerate higher stress and strain in the diagonal direction, though, to the cost of higher instabilities. The mechanical properties of each test are summarized in Table 5 as well as the average of each direction, including a final average of the material. It is interesting to note that the axial cutting direction shows a slightly higher Young's modulus, compared to the other directions, mostly likely resulting from the grain orientation.

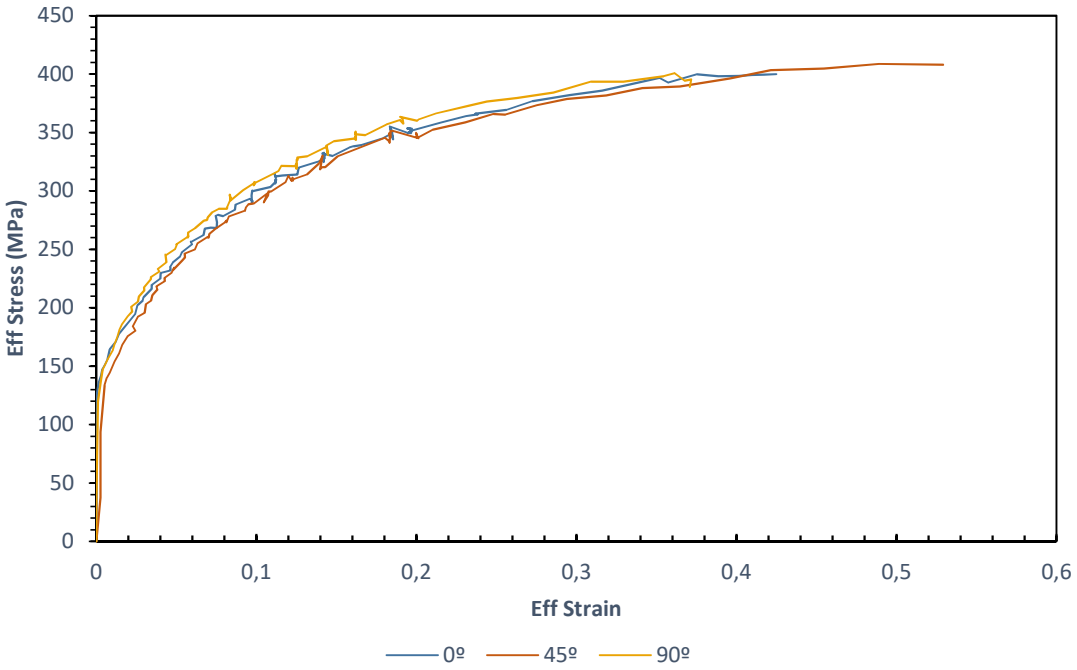

Figure 16: Effective stress-strain curves of a representative specimen of each direction.

Bringing a representative curve of each direction together (AlS500A, AlS545B, AlS590B) in Fig. 16 demonstrates that there is good correlation between the directions at intermediate and high strains. At lower strains, due to the very small deformations, the DIC readings show a higher fluctuation of strain values than the ones observed in the strain gauge readings. This effect originates from the noise captured by the camera that is then transmitted to the analysis software. However, as made clear in Fig. 17, where the strain gauge data of the same three tests is represented, the elastic region is virtually indistinguishable in the three directions. Furthermore, when analysing higher strains, the behaviour shows a much better correspondence to the DIC data, and the discrepancies remaining can be attributed to the

different placement of the strain gauge compared to the analysed necking region of the DIC and the problems discussed before arising from the DSA phenomenon. When accounting for the higher strains the major difference was already discussed previously, as the data clearly shows a higher failure strain in the 45º direction. It is also interesting to note that in the 90º direction, there is a higher stress resistance compared to the other directions, yet, it also represents the direction with the lower failure strain, indicating that there is a higher energy absorption earlier on during testing.

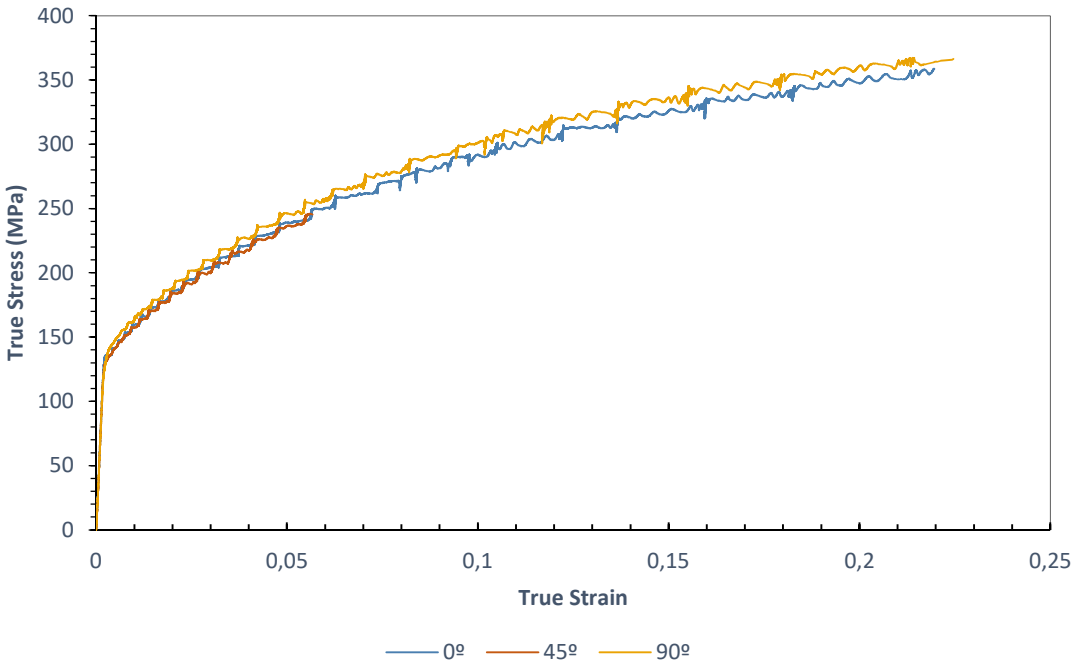

Figure 17: Strain gauge data from the tree tested cutting directions.

The Strain hardening parameters from the J-C flow constitutive model from Eq. (26) are tabulated in Table 6. These parameters were taken from the 0º direction test for its average behaviour representative of the material. The approximation was made by the minimum square fitting of a power law equation. The Cockcroft and Latham failure criterion (W_{cr}) parameter was calculated from the average area underneath the effective stress-strain curves.

Table 6: J-C strain hardening constitutive model and C-L failure criterion parameters.

Strain hardening			C-L Failure Criterion
A (MPa)	*B* (MPa)	*n*	*Wcr* (MPa)
130	620	0.6096	149

The strain hardening model is compared with the original curve in Fig. 18. The correlation at low strains is reasonable, however, as the strains increase there is a divergent behaviour, leading to an overestimation at the higher strains, but as reported by G. T. Gray III et. al [58], who also studied a version of the Al-5083 and the AL-7039, the J-C constitutive flow model offers the same problems for low strain rates and temperatures. Because this model is

empirical, and not a physical model of the material, it is expected that the results are an approximation to the real-world observations. Nevertheless, it has become one of the most common used models in impact simulation and its results have been considered acceptable in countless works, such as [14], [16], [18], [45], [59], [58].

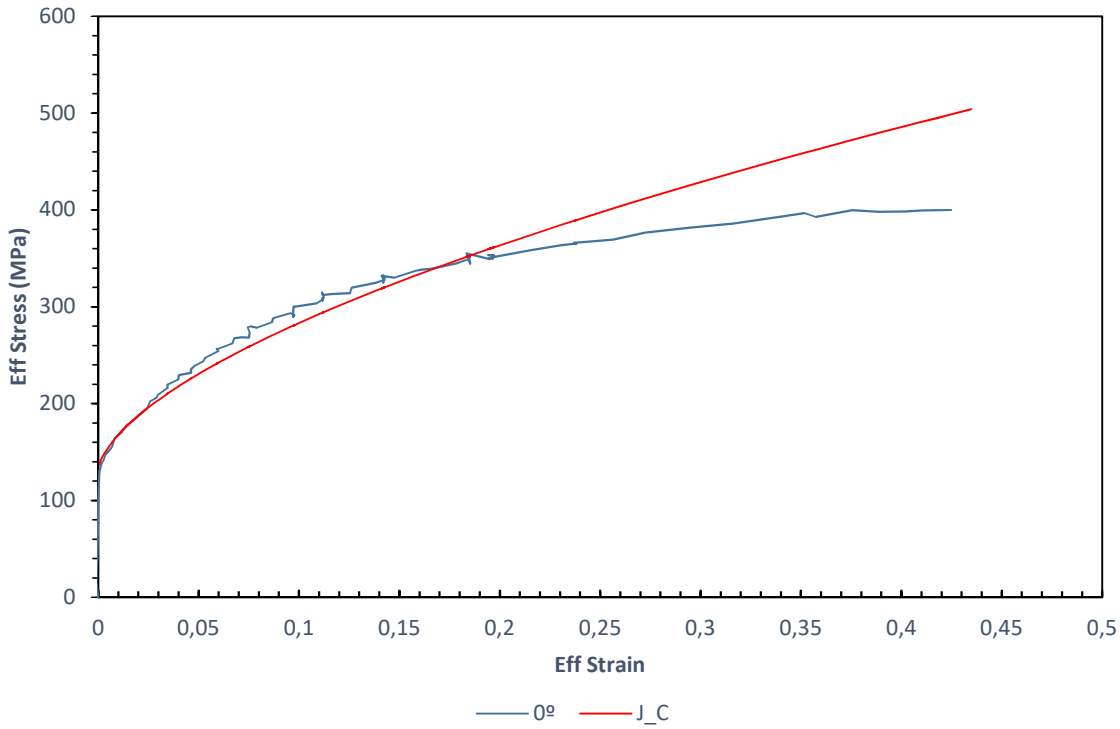

Figure 18: J-C strain hardening constitutive model compared to the experimental results for the 5 mm specimens.

4.1.2 10 mm Thick Specimens

It was also decided to test specimens of the same aluminium, with 10 mm thickness. The difference in thickness is tabulated to have lower yield strength and even slightly higher elongation [49]. As a solid plate might have different response to ballistic impacts as the same thickness of the same material comprised of several stacked layers, it is necessary to verify and determine the material constants and compare the results with the thinner specimens. The procedure is in everything similar for the exception that, due to the dimensions constraints, the tests were carried out in the *INSTRON 1341* as mentioned in 3.2.2. Therefore, some steps will be omitted in this chapter since they were already discussed previously.

In Fig. 19, the engineering stress-strain curve and the most significant steps are represented for the AlN1000B specimen. The behaviour does not diverge significantly from the thinner specimens' tests, and the DSA behaviour is still present. The DIC data is compared with the strain gauge data in Fig. 20, and again, a very good correlation is observed. The corrected tests results are presented in Fig. 21 and Table 7. Just as with the thinner specimens, the tests have very little variance within the same direction, and the highest yield strength, failure strength, and failure strain were observed in the 45º direction, although, the same instabilities with the

accentuated loss of load bearing capability well before rupture observed in the thinner specimens did not occur. Overall, the yield strength remains equal and the failure strength increased slightly, albeit, at lower failure strains. Another interesting factor is the higher Young's modulus exhibited by the thicker specimens, particularly, in the 0º direction. Just as with the thinner specimens, the 0º direction displays the higher Young's modulus from the three directions, confirming that the material offers more resistance to straining in the elastic region on the rolling direction.

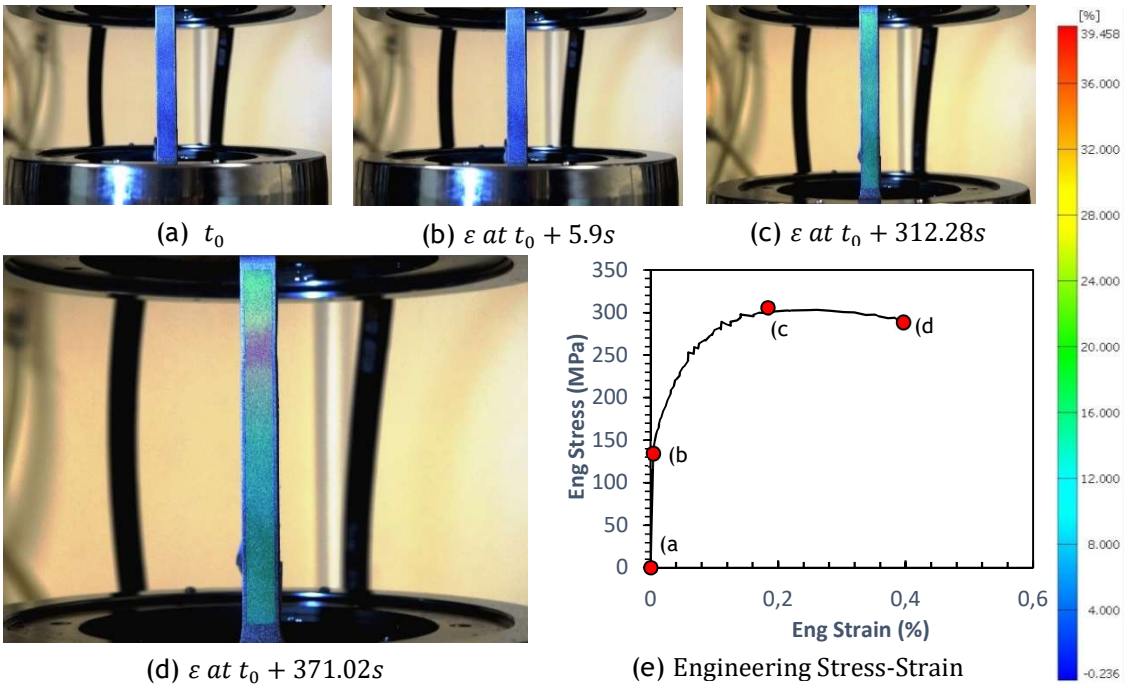

(a) t_0 (b) $\varepsilon\ at\ t_0 + 5.9s$ (c) $\varepsilon\ at\ t_0 + 312.28s$

(d) $\varepsilon\ at\ t_0 + 371.02s$ (e) Engineering Stress-Strain

Figure 19: GOM analysis of the AlN1000B Specimen loading axis strain at initial time (a), 0.2% Yield (b), maximum force (c) and just prior to rupture (d). (e) obtained engineering stress-strain curve.

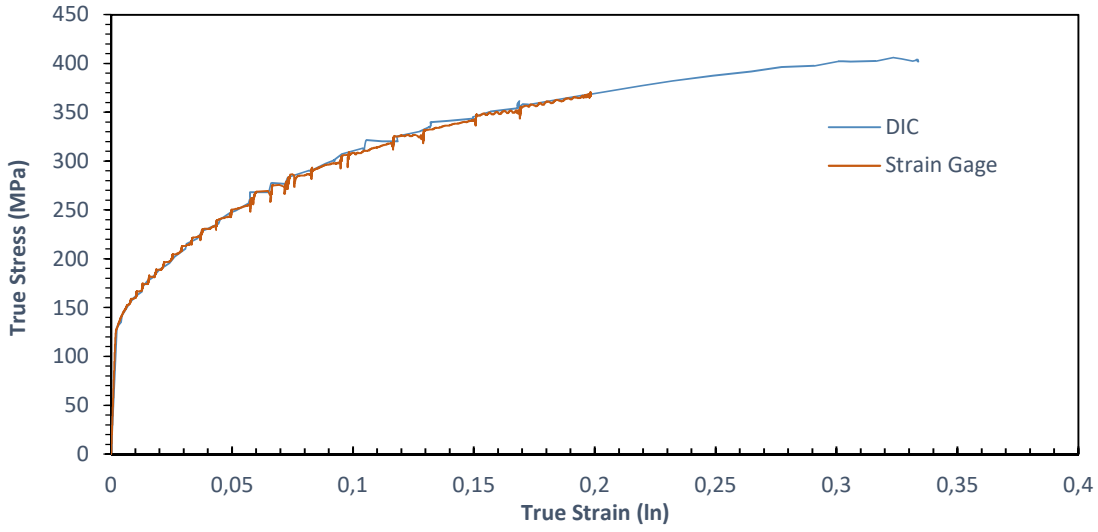

Figure 20: DIC obtained strains compared to strain gauge measurements of AlN1000B.

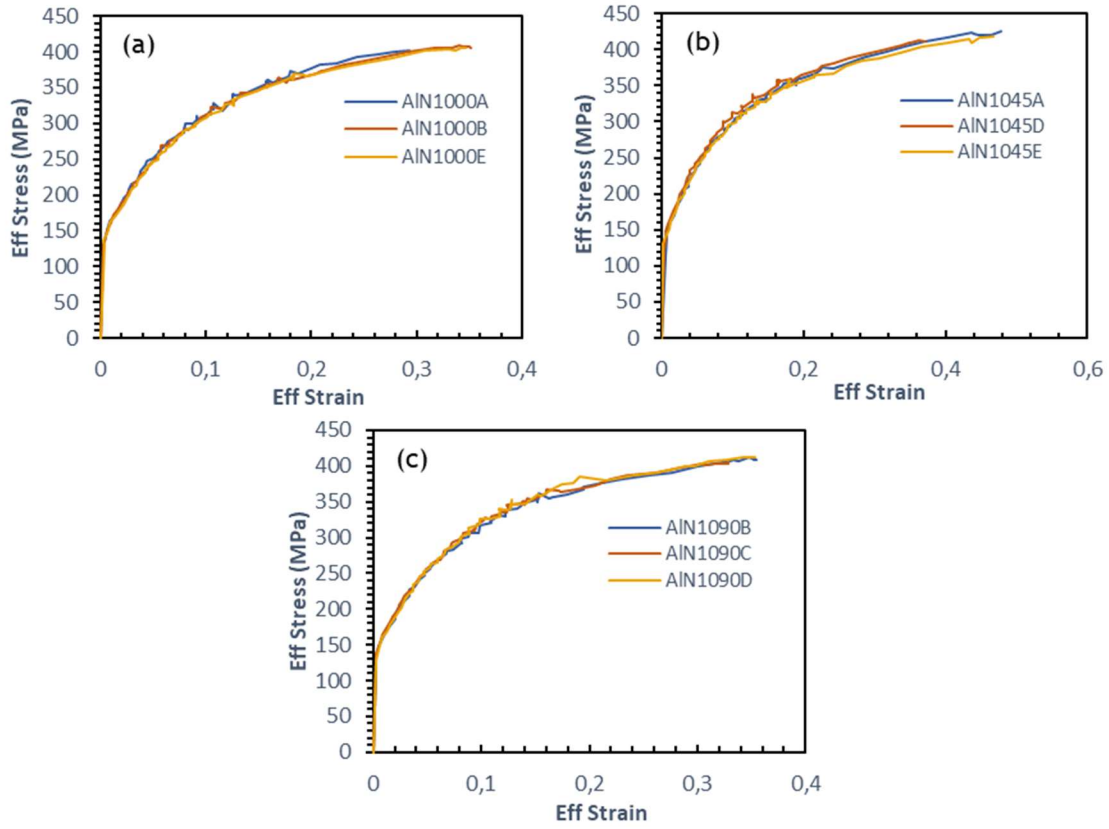

Figure 21: Corrected stress-strain curves from the 10 mm thick specimens; (a) 0° direction, (b) 45° direction and (c) 90° direction.

Table 7: Properties from the 10 mm thick specimens.

	Yield Strength 0.2% (MPa)	Tensile Strength (MPa)	E (GPa)	Poisson's Ratio	Elongation (%)	Failure Strain	W_{cr} (MPa)	Temp. (°C)
AlN1000A	137	402	71.7	0.313	23.94	0.31	95	18.9
AlN1000B	135	405	70.2	0.314	22.51	0.35	118	19.1
AlN1000E	135	406	71.8	0.313	23.47	0.35	115	19.1
Average	136	404	71.3	0.313	23.31	0.34	109	19.0
SD	1	1.73	0.73	0.0006	0.60	0.019	10.21	0.1
AlN1045A	144	425	66.6	0.462	26.92	0.48	167	21
AlN1045D	142	411	65.5	0.407	24.72	0.37	125	20.2
AlN1045E	132	418	67.8	0.322	29.78	0.47	161	20
Average	139	418	66.6	0.397	27.14	0.44	151	20.4
SD	5.26	5.72	0.94	0.06	2.07	0.05	18.55	0.43
AlN1090B	135	409	67.3	0.309	21.40	0.35	120	19.8
AlN1090C	138	407	68.7	0.307	20.46	0.33	110	19.6
AlN1090D	135	413	71.2	0.310	19.92	0.35	121	19.4
Average	136	410	69.1	0.309	20.59	0.35	117	19.6
SD	1.41	2.52	1.61	0.001	0.61	0.01	4.97	0.16
Total Average	137	410	69.0	0.34	23.68	0.37	130	19.6

E: Young's modulus; W_{cr}: Work per volume unit; SD: Standard deviation.

In these specimens, the *KFG-1-120-D16-11L3M3S* strain gauges were used, allowing for the retrieval of the Poisson's ratio. The average poisons ratio expected from AW-5083-H111 is 0.33 and despite a somewhat significant variation with testing direction, the average is very close at 0.34. It is interesting to note that the 45º cutting angle presented the highest Poisson's ratio indicating a significantly higher relation between the longitudinal contraction compared to the axial expansion in this direction, corroborating the higher axial strains observed with the DIC method.

Fig. 22 displays a representative effective stress-strain behaviour of each cutting direction, the AlN1000B, AlN1045A and AlN1090B. There are some similarities with the thinner specimens, however, now the axial and longitudinal directions have very similar stress sensitivity and very approximate failure strains. This indicates that there is more homogeneity in both directions compared to the thinner specimens. The 45º specimens have a higher failure strength just as seen before, however it also experiences lower stress resistance early on.

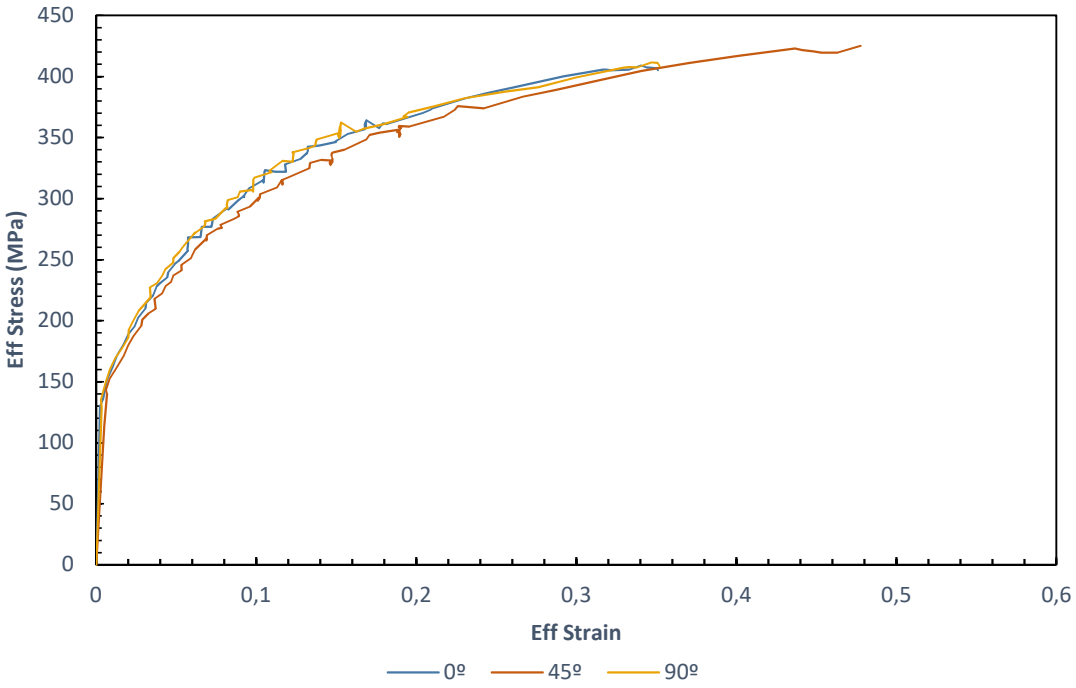

Figure 22: Effective stress-strain curves of a representative specimen of each direction.

Table 8: J-C strain hardening constitutive model and C-L failure criterion parameters.

Strain hardening			C-L Failure Criterion
A (MPa)	*B* (MPa)	*n*	*Wcr* (MPa)
110	610	0.5317	130

The J-C strain hardening coefficients and C-L Failure criterion are summarized in Table 8, and its representation compared to the 90º direction in Fig. 23. The approximation exhibits the same problems as with the thinner specimens with an overall poor approximation for the higher strains. The strain hardening behaviour is very similar to the thinner specimens nonetheless

(Fig. 24). Still, the work per volume unit is significantly lower on the thicker specimens, about 20 MPa lower, from 149 MPa to 130 MPa from the 5 mm to the 10 mm specimens, respectively.

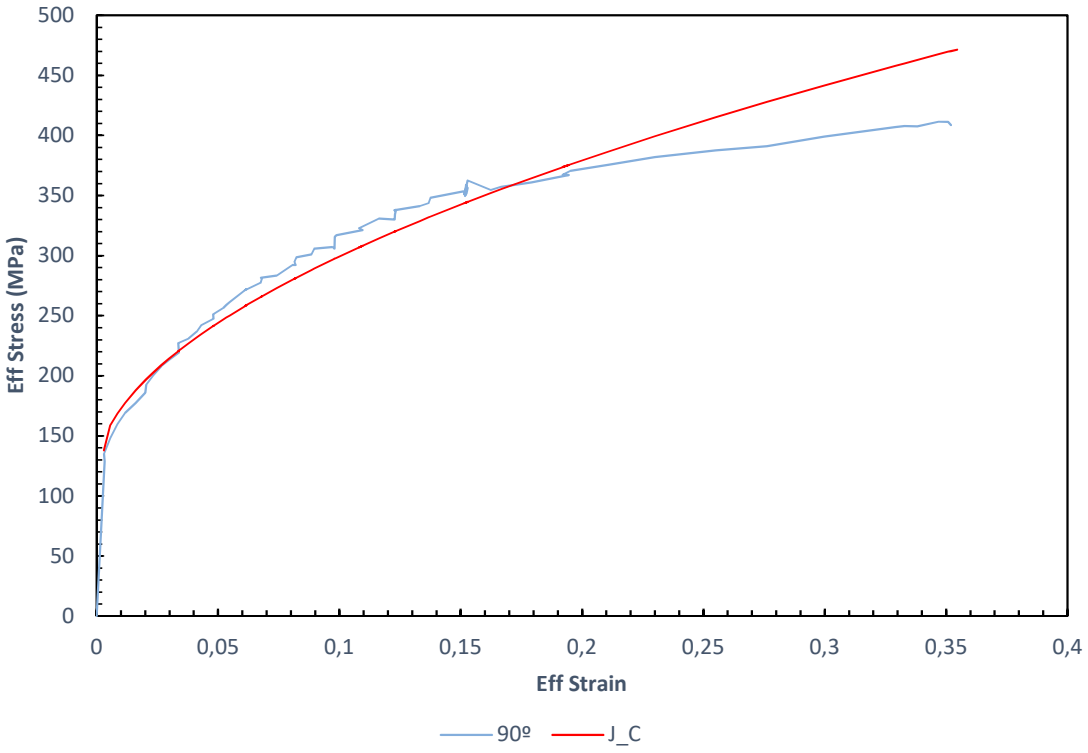

Figure 23: J-C strain hardening constitutive model compared to the experimental results for the 10 mm specimens.

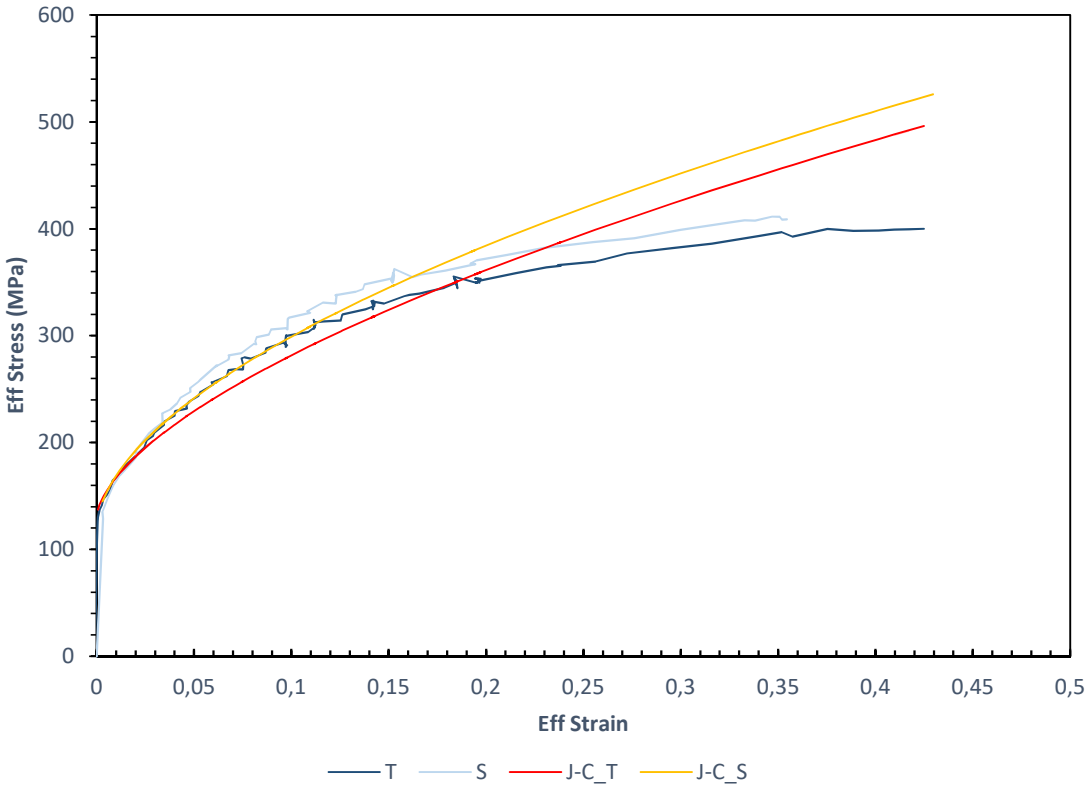

Figure 24: Comparison between the J-C Strain hardening models. T: 5 mm specimen; S: 10 mm specimen; J-C_T/S: Johnson-Cook Strain hardening models of the 5 and 10 mm specimens respectively.

Despite the similarity in behaviour, it is concluded that the difference in behaviour grants enough reason to use the different constitutive models when preforming computer simulations of the different thicknesses.

4.2 Ramor 500 Results

The other material selected for this project was the Ramor 500 from *SSAB*. Unlike the AW-5083, this armour steel doesn't have any defined J-C constitutive model in open literature, therefore, we can only compare the results to similar high hardness steels from literature.

In Fig. 25, the DIC analysis of the StS2.200E specimen is displayed alongside some of the most relevant stages of testing. Contrasting with the aluminium, no extraordinary phenomena was observed. The increase in strain and load bearing capabilities evolve in a very smooth and stable fashion. An interesting perspective arises from the fact that the highest percentage of deformation occurs on the last 40 seconds of a 218-second-long test in the necking region, while the rest of the specimen remains with very low deformation levels. This translates into interesting phenomena when we compare the two strain gauges data to the DIC obtained data as observed in Fig. 26.

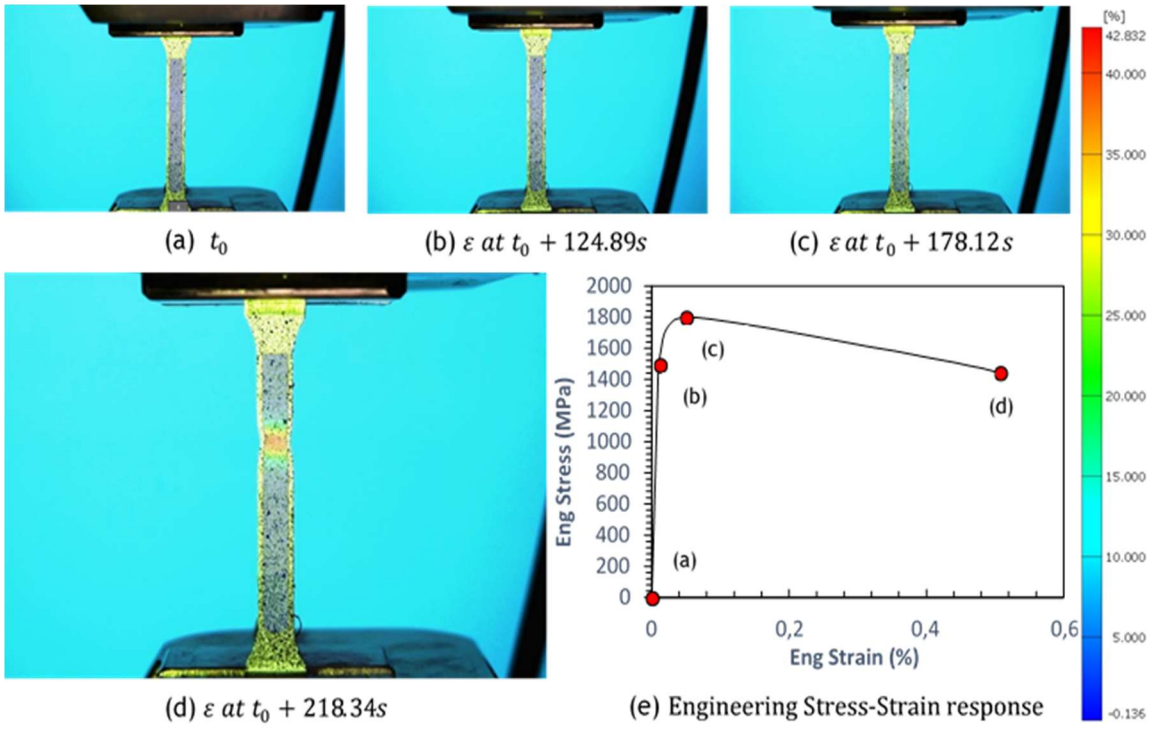

Figure 25: GOM analysis of the StS2.200E Specimen loading axis strain at initial time (a), 0.2% Yield (b), maximum force (c) and just prior to rupture (d). (e) obtained engineering stress-strain curve.

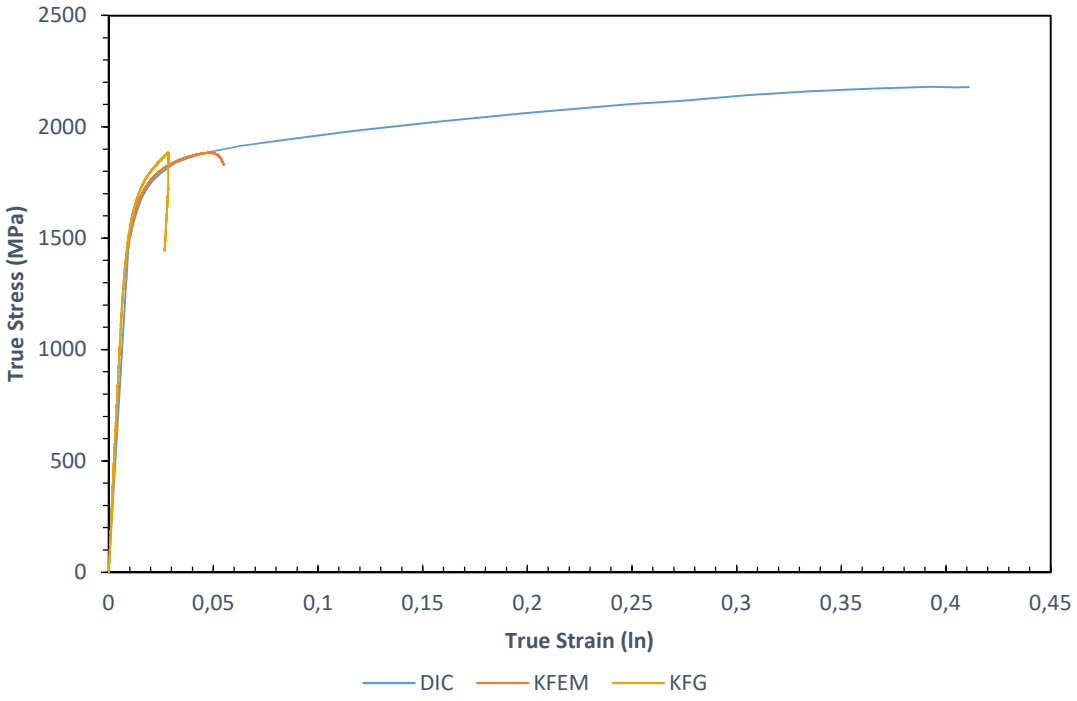

Figure 26: DIC obtained true strains compared to the KFEM and KFG strain gauge measurements of StS2.200E.

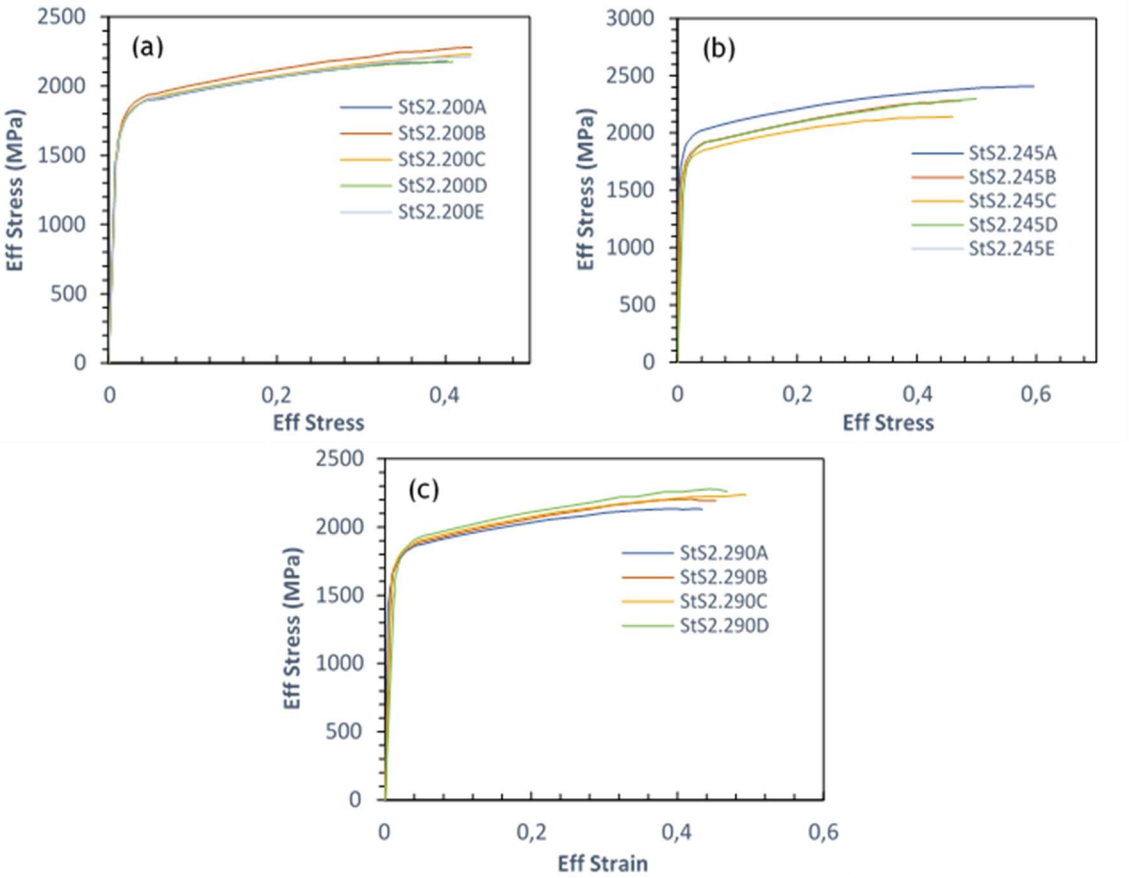

Figure 27: Corrected stress-strain curves from the Ramor 500 specimens; (a) 0° direction, (b) 45° direction and (c) 90° direction.

Table 9: Properties from the Ramor 500 specimens.

	Yield Strength 0.2% (MPa)	Tensile Strength (MPa)	E (GPa)	Poisson's Ratio	Elongation (%)	Failure Strain	W_{cr} (MPa)	Tempe. (ºC)
StS2.200A	1520	2170	192.1	0.273	5.62	0.40	810	19.5
StS2.200B	1620	2280	192.3	0.277	6.79	0.43	900	20
StS2.200C	1550	2230	193	0.273	7.58	0.43	880	20.2
StS2.200D	1560	2180	198.3	0.268	6.43	0.41	825	20.2
StS2.200E	1510	2210	191.5	0.275	6.33	0.43	870	20.2
Average	1550	2210	193.5	0.273	6.55	0.42	860	20
SD	38.73	39.5	2.48	0.003	0.64	0.01	34.13	0.27
StS2.245A	1700	2410	204.2	0.278	6.37	0.49	1340	19.1
StS2.245B	1600	2280	192.7	0.277	6.21	0.47	995	17.7
StS2.245C	1520	2140	186.4	0.277	7.06	0.46	920	18.4
StS2.245D	1530	2300	198.1	0.274	7.06	0.50	1040	18.8
StS2.245E	1520	2190	191.3	0.275	6.21	0.49	990	19.2
Average	1570	2260	194.5	0.276	6.58	0.48	1060	18.6
SD	69.86	93.6	6.10	0.001	0.39	0.01	146.65	0.55
StS2.290A	1360	2130	189.6	0.27	6.81	0.43	870	19.8
StS2.290B	1600	2190	191.4	0.273	6.82	0.45	925	20.1
StS2.290C	1630	2230	196.3	0.271	7.50	0.49	1020	20.5
StS2.290D	1630	2260	192.2	0.272	8.01	0.47	975	20.6
Average	1560	2200	192.4	0.271	7.28	0.46	950	20.2
SD	113.36	48.73	2.45	0.001	0.50	0.02	56.01	0.32
Total Average	1560	2230	195	0.274	6.80	0.45	955	19.6

E: Young's modulus; W_{cr}: Work per volume unit; SD: Standard deviation.

The StS2.200E is a very interesting case because the necking region formed very near the position where the high strain KFEM strain gauge was applied. This allows to compare the KFEM, KFG and DIC data in Fig. 26. While the KFEM strain gauge is almost a perfect match with the DIC data, the KFG data shows an overall lower strain levels early on the test, and after maximum load is reached, even a decrease in deformation is observed showing an elastic behaviour outside the necking region. This also indicates that the necking region, in this case, is determined early on during testing. The KFEM strain gauge data, after the maximum load, is unable to keep track of the deformation exhibiting a decrease in stress becoming unglued soon after.

The corrected results from all the tests, and the material properties obtained are presented in Fig. 27 and Table 9 respectively. Overall there is very good correlation between the tests with increasing variation towards the rupture point, although, with the oblique cutting direction presenting three almost indistinguishable tests, one with exceptionally high stress and high strain tolerance (StS2.245A) and one with exceptionally low stress and low strain tolerance (StS2.245C). This direction, as with the experienced with the aluminium, also exhibits the higher failure strains, even though, the failure stress is, on average, very similar. One interesting observation is that, despite, having an above average failure strain, the oblique direction does not have the highest elongation, being this factor considerably higher with the

perpendicular cutting direction. This suggests that the 45º direction experiences higher reduction in strain on the non-necking region, possibly originating some instabilities and resulting in the higher dispersion of the tests.

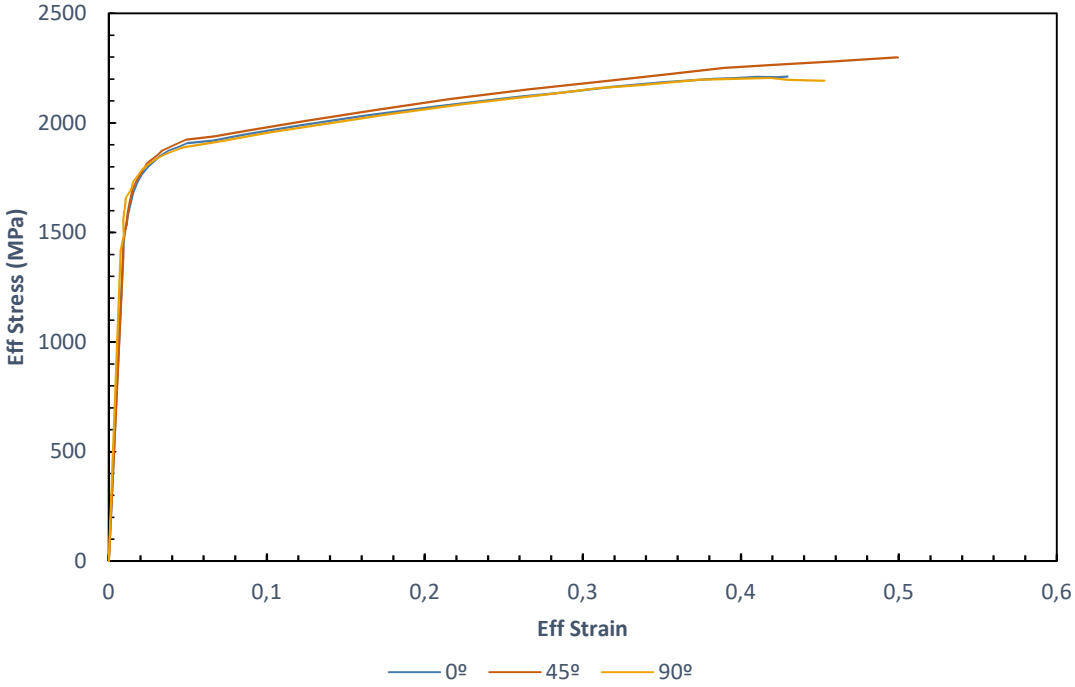

Figure 28: Effective stress-strain curves of a representative specimen of each direction.

Table 10: J-C strain hardening constitutive model and C-L failure criterion parameters.

Strain hardening			C-L Failure Criterion
A (MPa)	*B* (MPa)	*n*	*Wcr* (MPa)
1530	880	0.3114	955

The representation of the average behaviour of the three cutting directions is exhibited in Fig. 28. The 0º, 45º and 90º directions are represented by the StS2.200E, StS2.245D and StS2.290B respectively, and it is clear that, despite the failure strain, the behaviour of the Ramor is very similar in the three directions.

The J-C strain hardening constitutive model and C-L failure criterion are displayed in Table 10, and the graphical representation is compared to the StS2.290B specimen stress-strain relationship in Fig. 29. It must be addressed that, in order to obtain a better approximation from the strain hardening behaviour, it was decided that the regression would disregard the data closer to the yield strength. By doing so, the representation slightly overestimates the behaviour close to the Yield strength but, can maintain a very close representation of the high strain response, obtaining a much better estimate than with the aluminium. The same method was not applied then due to the higher curvature of the stress-strain relationship, meaning that if a conversion to higher strains was attempted, the overestimation for lower strains would be much greater. Therefore, only the steel can benefit from this approach.

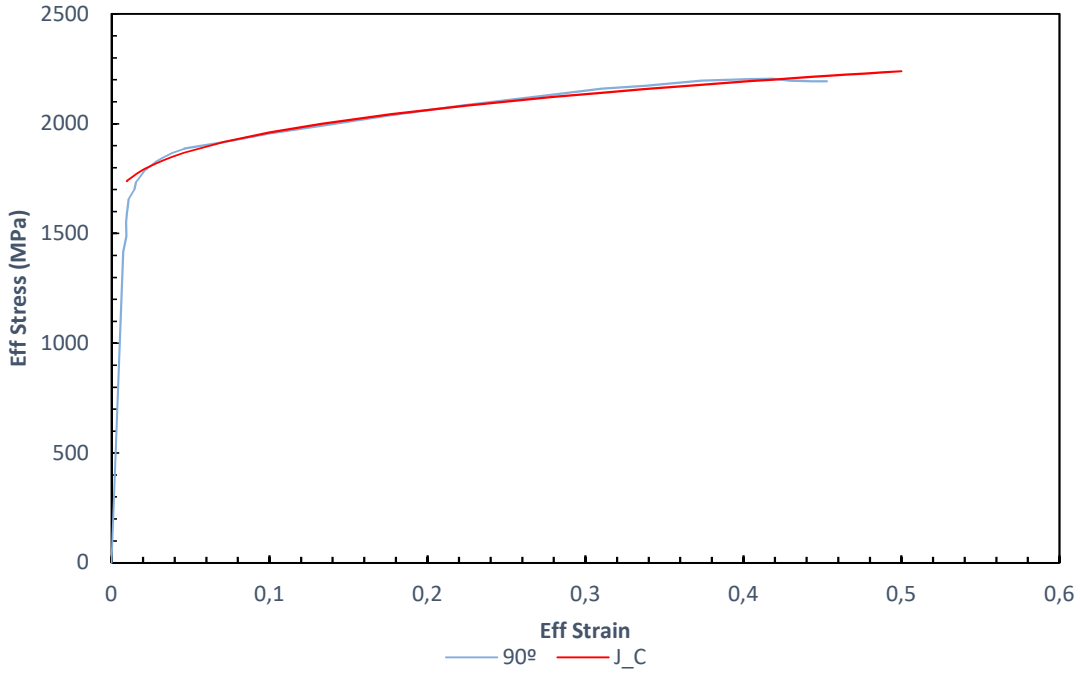

Figure 29: J-C strain hardening constitutive model compared to the experimental results for the 90º reference specimen.

Table 11: J-C strain hardening constitutive model constants for several 500 HB steels.

	Hardness	Yield	Tensile	Strain hardening		
	HB	(MPa)	(MPa)	A (MPa)	B (MPa)	n
Domex protect 500 [59]	477-550	1500	1800	2030	504	1
Armox 500T A [60]	480-540	1250 min	1450-1750	1470	702	0.199
Armox 500T B [61]				849	1340	0.092
Secure 500 A [62]	480-530	1300	1600	1299	2230	0.5585
Secure 500 B [46]				1270	1580	0.0038

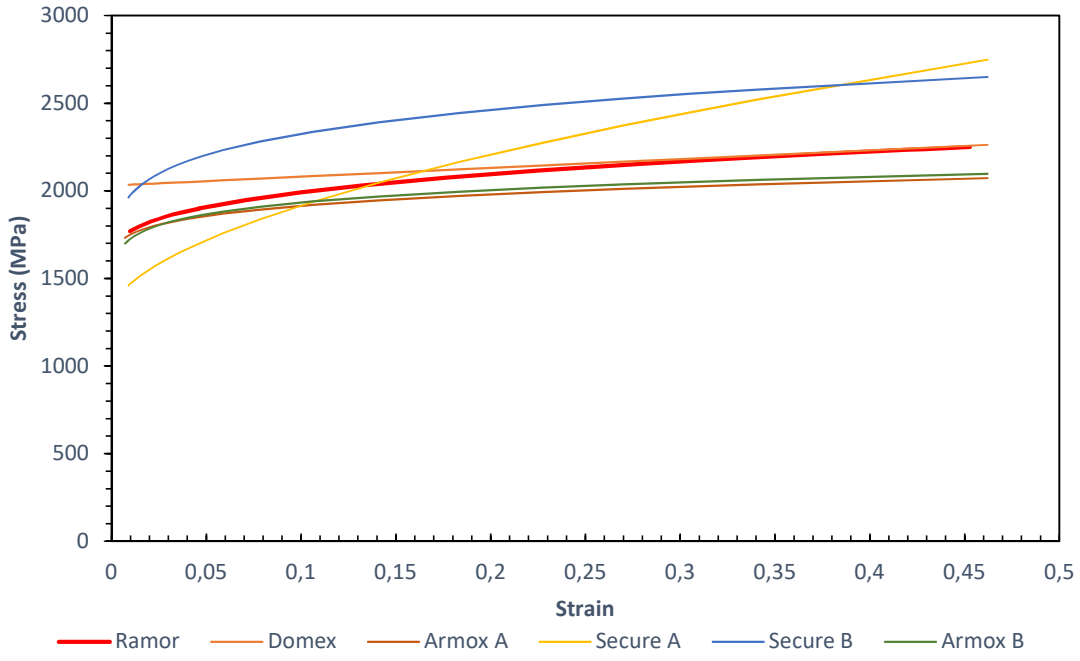

Figure 30: Comparison of the obtained Ramor 500 J-C model with similar steels from literature.

In the literature, it is possible to find a few J-C constitutive models for similar 500 HB hardness level steels, namely, Domex Protect 500 [59], Armox 500 T A [60] and B [61], Secure 500 A [62] and B [46], and their respective parameters are tabulated in Table 11. Comparing the obtained results with these high hardness steels (Fig. 30), shows good agreement with the general data from the literature, boosting confidence on the experimental data obtained.

4.3 Application perspectives

Based on the obtained stress-strain behaviour of the tested alloys it is possible to estimate the performance and suitable role each material could fulfil in an armour solution. Since the tested aluminium alloy has already seen use in armoured transport vehicles and one of its major advantages is the energy absorption capabilities compared to its low density face steel alloys, the simple application of a single plate, or a multi-layered plate, comprised of this metal should provide sufficient protection for small fire arms, but poor protection against AP rounds and blast waves. However, if incorporated in a sandwich system, either by composing the faces of a viscoelastic core, or by serving as a spall liner of a ceramic or hardened steel face, this aluminium could provide a much more effective solution than either of these parts isolated.

Due to the high levels of hardness of the tested steel, its strongest advantage in an armour solution would be as an impactor face. It would be able to erode and possibly even fragmentate the impactor absorbing a great amount of energy in the process, allowing for a softer material to more successfully dissipate the remaining kinetic energy. Though this function can be performed by a ceramic, the steel would be a cheaper alternative while providing better multi-hit performance.

5 Conclusions and Future Research

In this study, the quasi-static true stress-strain relationships of flat specimens of armour graded aluminium and steel alloys have been determined experimentally by resorting to a digital image correlation method. This was achieved by measuring the load, width reduction and strain fields on the surface and centre of the neck through a modern digital camera, and posteriorly applying a correction factor to take into account the thickness reduction. From the data obtained in this study, the following conclusions can be drawn:

- The digital image correlation technique used in this study provides satisfactory results when compared to the strain gauge data.
- The dynamic strain aging phenomena observed in the studied aluminium is also observed in the DIC data, however, the smaller serrations require a higher number of stages and a higher resolution camera to be observed.
- There are some noticeable differences in the different cutting directions of the materials, in particular, the 45-degree cut in the aluminium specimens experiencing on average higher failure strains, and sometimes even a long and slow decrease in stress bearing ability prior to complete rupture.
- The observation was made that there are some differences in stress-strain behaviour with different thicknesses of the same material, granting each the necessity of its own material constants.
- The Johnson-Cook strain hardening constitutive model only offers an approximation to the true stress-strain relationship observed experimentally, though having much better correspondence with the steel data compared with the aluminium.
- The homemade installation used in this study provides satisfactory results when compared to the results obtained with similar works in open literature.

This work was part of a partnership intended to find the results of adding cork to an armour solution incorporating the tested materials. The current work is only able to set the first steps in the full realization of the project and thus, a set of steps to fully realize the project goals are suggested. So, for future works intended to assert the full mechanical characterisation of the materials in order to obtain good numerical simulations, a series of tests should be performed. These should include tensile tests with higher strain rates and dynamic tests on split Hopkinson bars for the analysis of extremely high strain rates. These tests would allow for the full determination of the constants for the Johnson-Cook material model, including the J-C cumulative damage model.

After the appropriate material characterization is attained, the numerical simulations of ballistic impacts on each material, and combinations of them, using commercially available software such as Abaqus and LS-DYNA would be the next step.

Finally, the application of the cork on the core of a sandwich composed of the best solutions would be numerically simulated and compared to the results of the models without cork implementation. If the data showed promising results, then the production and testing of real specimens should be the final step in the project.

References

[1] S. Sanchez-Saez, E. Barbero and J. Cirne, “Experimental study of agglomerated-cork-cored structures subjected to ballistic impacts,” *Materials Letters,* 2011.

[2] J. Sousa-Martins, D. Kakogiannis, F. Coghe, B. Reymen and F. Teixeira-Dias, “Behaviour of sandwich structures with cork compound cores subjected to blast waves,” *Engineering Structures,* vol. 46, pp. 140-146, 2012.

[3] J. Sousa-Martins, D. Kakogiannis, F. Coghe, B. Reymen and F. Teixeira-Dias, “Response of cork compounds subjected to impulse blast loads,” *The European Physical Journal,* vol. 206, pp. 61-70, 2012.

[4] N. S. Franco, “Caracterização mecânica de um material híbrido de Carbono/Epoxy e cortiça,” Covilhã, 2009.

[5] *Pen Drawing of Armoured Car.* [Performance]. 1487.

[6] The Autocar, “The Simms "Motor Scout.",” *THE AUTOCAR,* p. 761, 26 August 1899.

[7] The Engineer, “Self-propelled war car,” *THE ENGINEER,* p. 368, 11 April 1902.

[8] R. Ogorkiewicz, Tanks: 100 years of evolution, Bloomsbury Publishing, 2015.

[9] A. G. Stern, Tanks: 1914-1918, London: Hodder and Stoughton, 1919.

[10] T. L. H. Butterfield, “Design and Development of Fighting Tanks,” *Proceedings of the institution of Mechanical Enginners: Automobile Division,* pp. 159-189, 1965.

[11] M. Übeyli, R. O. Yildirim and B. Ögel, “On the comparison of the ballistic performance of steel and laminated composite armors,” *Materials and Design,* vol. 28, pp. 1257-62, 2007.

[12] J. Manganello and K. H. Abbott, “Metallurgical factors affecting the ballistic behaviour of steel targets.,” *J Mater,* vol. 17, pp. 231-9, 1972.

[13] S. E. Schoenfeld and T. W. Wright, “A failure criterion based on material instability,” *International Journal of Solids an Structures,* vol. 40, pp. 3021-3037, 2003.

[14] T. Demir, M. Übeyli and R. O. Yildirim, “Investigation on the ballistic impact behaviour of various alloys against 7.62mm armor piercing projectile,” *Materials and Design,* vol. 29, pp. 2009-2016, 2008.

[15] N. K. Gupta and V. Madhu, “An experimental study of normal and oblique impact of hard-core projectile on single and layered plates,” *International Journal of Impact Energy,* vol. 17, pp. 395-414, 1997.

[16] E. A. Flores-Johnson, M. Saleh and L. Edwards, “Ballistic performance of multi-layered metallic plates impacted by a 7.62-mm APM2 projectile,” *International Journal of Impact Engineering,* vol. 38, 2011.

[17] S. Dey, T. Børvik, X. Teng, T. Wierzbicki and O. S. Hopperstad, “On the ballistic resistance of double-layered steel plate: An experimental and numerical investigation,” *International Journal of Solids and Structures,* vol. 44, 2007.

[18] P. J. Hazell, Armour Materials, Theory and Design, CRC Press, 2015.

[19] C. B. Salter and H. Spiro, Evaluation of siliceous cored armor for the XM60 tank, Michigan: Metals Section, Materials branch Recsearch and Development Division, 1958.

[20] M. R. O'Masta, V. S. Deshpande and H. N. G. Wadley, “Mechanisms of projectile penetration in Dyneema encapsulated aluminium structures,” *International Journal of Impact Engineering ,* vol. 74, pp. 16-35, 2014.

[21] R. L. Cook, “Hard faced ceramic and plastic armor”. United States of America Patent 3,509,833, 5 May 1970.

[22] M. Wilkins, C. Honodel and D. Sawle, “An approach to the study of light armor,” Lawrence Radiation Laboratory, Livermore, 1967.

[23] A. L. Florence and T. J. Ahrens, “Interaction of projectiles and composite armor,” U.S. Army Materials Research Agency, Watertown, Massachusetts, 1967.

[24] A. L. Florence, “Interaction of projectiles and composite armor Part II,” Army Materials and Mechanics Research Center, Watertown, Massachusetts, 1969.

[25] M. Übeyli, O. Yildirim and B. Ögel, “Investigation on the ballisitic behaviour of AL2O3 laminated composites,” *Journal of Materials Processing Technology,* vol. 196, pp. 356-364, 2008.

[26] K. Dateraksa, K. Sujirote, R. Mccuiston and D. Atong, “Ballistic performance of ceramic/S2-glass composite armor,” *Journal of Metals, Materials and Minerals,* vol. 22, pp. 33-39, 2012.

[27] Commitee on Opportunities in Protection Materials Science and Technology for Future Army Applications; National Materials Advisory Board; Board on Army Science and Technology; Division on Engineering and Physical Sciences; National Research Council, Opportunities in Protection Materials Science and Technology for Future Army Applications, Washington, D.C.: The National Academies Press, 2011.

[28] A. P. Mouritz, E. Gellert, P. Burchill and K. Challis, “Review of advanced composite structures for naval ships and submarines,” *Composite Structures,* vol. 53, pp. 21-41, 2001.

[29] D. Fecko, “High strength glaasreinforcements still being discovered,” *Reinforced Plastics,* vol. 50, pp. 40-44, 2006.

[30] R. Bird, “Protection of Vehicles against Landmines,” 2001.

[31] S. Follett, “Ballistic analysis of composite V-shaped hulls: An experimental and numerical aproach,” Cranfield University, Cranfield, 2011.

[32] Global Security, “Improvised Explosive Devices (IEDs) / Booby Traps,” 05 07 2011. [Online]. Available: http://www.globalsecurity.org/military/intro/ied.htm. [Accessed 17 09 2016].

[33] T. Rahimzadeh, E. M. Arruda and M. D. Thouless, “Design of Armor for Protection against Blast and Impact,” *Journal of the Mechanics and Physics of Solids,* 2015.

[34] E. Wang, N. Gardner and A. Shukla, “The blast resistance of sandwich composites with stepwise graded cores,” *International Journal of Solids and Structures,* vol. 46, pp. 3492-3502, 2009.

[35] N. Gardner, E. Wang and A. Shukla, “Performance of functionally graded sandwich composite beams under shock,” *Composite Structures,* vol. 94, pp. 1755-1770, 2012.

[36] H. Pereira, Cork: biology, production and uses., vol. 1st ed, Elsevier, 2007.

[37] B. K. Fink and J. W. Gillespie, Jr, “Cost-Effective Manufacturing of Damage-Tolerant Integral Armor,” Army Research Laboratory, Aberdeen Proving Ground, 2000.

[38] B. K. Fink, A. M. Monib and J. W. Gillespie, jr, “Damage tolerance of thick-section composites subjected to ballistic impact,” Army Research Laboratory, Aberdeen Proving Ground, 2001.

[39] B. A. Gama, J. W. Gillespie Jr., T. A. Bogetti and B. K. Fink, “Innovative design and ballistic performance of lightweight composite integral armor,” in *SAE Technical Papers*, Detroit, Michigan, 2001.

[40] I. Scheider, W. Brocks and A. Cornec, “Procedure for the determination of true stree-strain curves from tensile tests with rectangular cross section specimens,” *Journal of Engineering Materials and Technology,* vol. 126, pp. 70-76, 2004.

[41] M. M. Ahmmad and Y. Sumi, “Strenght and deformability of corroded steel plates under quasi-static tensile load,” *Journal of Marine Science Technology,* vol. 15, pp. 1-15, 2010.

[42] P. W. Bridgman, Studies in large plastic flow and fracture, Cambridge: Harvard University Press, 1964.

[43] A. A. Ostsemin, “Stress in the least cross section of round and plane specimens,” *Strength Mater 24,* vol. 4, pp. 298-301, 1992.

[44] E. E. Cabezas and D. J. Celentano, “Experimental and numerical analysis of the tensile test using sheet specimens,” *Finite Element in Analysis and Design,* vol. 40, pp. 555-575, 2004.

[45] G. R. Johnson and W. H. Cook, “A constitutive model and data for metals subjected to large strains, high strain rates and high temperatures,” Hague, Netherlands, 1983.

[46] N. Kiliç and E. Bülent, “Ballistic resitance of high hardness armor steels against 7.62 mm armor piercing ammunition,” *Materials and Design,* vol. 44, pp. 35-48, 2013.

[47] M. G. Cockcroft and D. J. Latham, “Ductility and the workability of metals,” *Journal of the Institute of Metals,* vol. 96, 1968.

[48] SSAB, “www.ssab.com,” 2017. [Online]. Available: https://www.ssab.com/products/brands/armox/ramor-500. [Accessed 26 10 2017].

[49] Aalco Metals Limited, “www.aalco.co.uk,” 12 07 2016. [Online]. Available: http://www.aalco.co.uk/datasheets/Aluminium-Alloy-5083-0-H111-Sheet-and-Plate_149.ashx. [Accessed 26 10 2017].

[50] ruuki, “www.ruuki.com,” 2012. [Online]. Available: https://oxycoupage.com/FichiersPDF/Ruukki_Pdf/English/ Ruukki-Ramor-protection-steels-hand-out-10-2012.pdf. [Accessed 22 07 2018].

[51] MatWeb, “www.Matweb.com,” MatWeb, [Online]. Available: http://www.matweb.com/search/datasheet.aspx?matguid=ee25302df4b34404b21ad67f8a83e858&n=1&ckck=1. [Accessed 22 07 2018].

[52] ASTM E 8M-04, “Standard Test Method for Tension Testing of Metallic Materials”.

[53] G. GmbH, “gom.com,” GOM GmbH, [Online]. Available: https://www.gom.com. [Accessed 18 04 2018].

[54] G. T. Motsi, B. M. Shongwe, T. J. Sono and A. P. Olubambi, “Anisotropic behaviour studies of aluminum alloy 5083-H0 using a micro-tensile test stage in a FEG-SEM,” *MAterials Science & Engineering A,* vol. 656, pp. 266-274, 2016.

[55] F. Kabirian, A. S. Khan and A. Pandey, “Negative to positive strain rate sensitivity in 5xxx series aluminum alloys: Experiment and constitutive modeling,” *International Journal of Plasticity,* vol. 55, pp. 232-246, 2014.

[56] K. Chihab, H. Ait-Amokhtar and K. Bouabdellah, “Serrated yielding due to Portevin-Le Chatelier in commertial AL-Mg alloys,” *Annales de Chime Science des Matériaux,* vol. 27, pp. 69-75, 202.

[57] A. Benallal, T. Berstad, T. Børvik, O. S. Hopperstad, I. Koutiri and R. Nougueira de Codes, “An experimental and numerical investigation of the behaviour of A5083 aluminium alloy in presence of the Portevin-Le Chatelier effect,” *International Journal of Plasticity,* vol. 24, pp. 1916-1945, 2008.

[58] G. T. Gray III, S. R. Chen, W. Wright and M. F. Lopez, “Constitutive Equations for annealed Metals Under Compression at High Strain Rates and High Temperatures,” Los Alamos National Laboratory, Los Alamos, New Mexico, 1994.

[59] T. Børvik, S. Dey and A. H. Clausen, “Perforation resistance of five different high-strength steel plates subjected to small-arms projectiles,” *International Journal of Impact Engineering ,* vol. 36, 2009.

[60] P. Skoglund, M. Nilsson and A. Tjernberg, “Fracture modeling of a high performance armour steel.,” *J. Phys.,* vol. 134, no. IV France, pp. 197-202, 2006.

[61] M. Nilsson, “Constitutive model of Armox 500 T and Armox 600T at low and medium strain rates,” Weapons and Protection, Swedish Defence Research Agency (Vapen och skydd, Totalförsvarets forskningsinstitut (FOI)), 2003.

[62] N. Nsiampa, F. Coghe and G. Dykmans, “Numerical investigation of the bodywork effect,” *DYMAT,* pp. 1561-6, 2009.

Appendixes

Appendix A

LabView Block Diagram